

Ultrafast structural dynamics of VO₂

Sergiy Lysenko,* Nardeep Kumar, Armando Rúa, José Figueroa, Junqiang Lu, and Félix Fernández

Department of Physics, University of Puerto Rico, Mayaguez, Puerto Rico 00681, USA

(Received 6 February 2017; revised manuscript received 27 July 2017; published 14 August 2017)

Distinct contribution of acoustic and optical phonons in light-induced lattice transformation was resolved at different time scales by monitoring the insulator-to-metal phase transition in epitaxial and nonepitaxial VO₂ films. Applying the ultrafast angle-resolved light scattering technique we demonstrate a significant influence of internal misfit strain in epitaxial films on subpicosecond phase transition dynamics. This technique also allows for observing a contribution of structural defects in the evolution of the transient state. The ultrafast structural phase transition dynamics is discussed in terms of the Ginzburg-Landau formalism. Using a set of experimental data we reconstruct the thermodynamic potential of photoexcited VO₂ and provide a phenomenological model of the ultrafast light-induced structural phase transition.

DOI: [10.1103/PhysRevB.96.075128](https://doi.org/10.1103/PhysRevB.96.075128)

I. INTRODUCTION

Vanadium dioxide is a classic example of a ferroelastic material that undergoes first-order insulator-to-metal transition (IMT) at temperature $T_c = 341$ K [1]. The transition is accompanied by structural change [2,3] from low-temperature monoclinic (M_1 structure, space group C_{2h}^5) [4,5] to high-temperature rutile (R structure, space group D_{4h}^{14}) [6] lattice symmetry. Owing to strong electron correlations, the phase transition dynamics of VO₂ is a very complex process. Crystallinity and internal strain significantly alter the width and tilt of thermal hysteresis and can shift the temperature of IMT by several degrees above or below the T_c point of stoichiometric unstrained VO₂ crystal [7,8]. Numerous theoretical approaches have been developed to describe VO₂ phase stability. While some models explain the metal-insulator transition in terms of the Mott-Hubbard mechanism of correlation gap opening [9–12], other approaches consider band models with Peierls instability [13–15] or describe it by combining both mechanisms [16–18]. Moreover, all these substantially different approaches provide fairly close qualitative and quantitative explanations of VO₂ physical properties. Therefore, in order to better understand the actual mechanisms of IMT in VO₂, along with theoretical approaches, new experimental methods are required to track the process dynamics.

While the IMT of VO₂ can be induced by heat, this transition can be also initiated or altered by strain [8,19–22], electric current [23–25], by doping with different metal ions [26,27], by THz radiation [28], and by light [29–34]. The investigation of ultrafast photoinduced processes in phase-change materials is of special interest since methods of ultrafast spectroscopy can potentially track electron and phonon lattice dynamics separately. Existing theoretical models provide a satisfactory description of ultrafast dynamics of photoexcited VO₂ [35–37]. However, these models also reveal the great complexity of the problem, and the general picture of evolution for electronic and lattice subsystems is still poorly understood. The problem of the nature of photoexcited states remains open. In most cases, experimental and theoretical studies assume for simplicity only the photogeneration of dense electron-hole

plasma but neglect the possibility of excitonic and polaronic states in VO₂.

As shown in numerous works [22,38–45], the photoinduced IMT in VO₂ depends on incident light intensity, wavelength, and also on film crystallinity, structural defects, and internal strain. Recent studies indicate that the ultrafast structural phase transition (SPT) is likely to be triggered by a screening of electron correlations on the subpicosecond scale [34,36,46,47]. The study of ultrafast response in VO₂ by Mayer *et al.* [28] shows that the subpicosecond nonthermal IMT of VO₂ can also be induced by a strong THz pulse. Since the THz excitation does not produce direct photodoping, the proposed model of the IMT involves carrier tunneling in the presence of strong THz field. We note that the utilization of strong THz field for triggering and monitoring the IMT in VO₂ is of special interest since it can provide new information about bonded electronic states, cooperative effects and the possible presence of polaronic states [10,48], and their role in structural and electronic properties of VO₂.

In this paper, we demonstrate a comprehensive approach describing the pathways of photoinduced first-order structural transition in VO₂ versus the optical excitation level, material strain, morphology, and structural defects. The discussion starts by presenting a semiclassical computation (Sec. II) of vibration density of states and adiabatic relaxation of kinetic energy on the subpicosecond time scale. We apply a method of molecular dynamics (MD) which neglects electron-electron correlations and, therefore, simulates the actual case of photoinduced screening of the correlations. In order to better understand the results of MD computation and to find relations between different degrees of freedom of ultrafast structural dynamics, we performed the experimental study of VO₂ with techniques described in Sec. III. In Sec. IV we report on the experimental results of time-resolved transmission, reflection, and angle-resolved light scattering within nanosecond, picosecond, and subpicosecond time scales. We show a noticeable influence of photoacoustic strain on nonlinear optical (NLO) dynamics of VO₂ on the nanosecond time scale. Then, applying the time-resolved light scattering technique, we observe a grain-size-dependent phase transition on the subpicosecond time scale at different levels of optical excitation. The dynamics of photoinduced SPT shows a considerable anisotropy for epitaxial VO₂ film due to influence of the misfit

*sergiy.lysenko@upr.edu

strain. The evolution of the excited state depends on the size of VO₂ grains/domains and on concentration of structural defects. In Sec. V we summarize our experimental data and present a phenomenological model of ultrafast structural dynamics of VO₂. Our modeling is based on the numerical integration of the equation of motion for the effective displacement of lattice ions in terms of Ginzburg-Landau formalism.

II. SUBPICOSECOND MOLECULAR DYNAMICS

Recent progress in experimental and theoretical studies of phase transition in VO₂ evidences that the screening of electron correlations is a key factor which triggers the SPT [12,18,34,36,46]. Photoinduced metallization of VO₂ occurs during the light pulse interaction, showing Mott-type behavior with possible band-gap collapse on a time scale less than ~ 60 fs [46,49]. Nevertheless, the total structural transformation of VO₂ lattice from monoclinic to rutile symmetry is slower with durations ranging from ~ 80 fs to several hundred femtoseconds [39] or even several picoseconds [50–52], depending on the level of optical excitation, wavelength, and morphology of the sample. In this context, the transient lattice distortion can be modeled by using semiclassical computational methods of molecular dynamics (MD) which neglect electron-electron correlations. We note that the MD method does not permit computation of exact lattice dynamics during SPT, but provides a meaningful estimation of quantitative parameters of these dynamics [i.e., root-mean-square (rms) atomic displacements, vibrational density of states, kinetics of energy relaxation, etc.].

To compute the MD we used the QUANTUMWISE software package [53]. The method of MD employs the Born-Oppenheimer approach with semiclassical ReaxFF (reactive force field) potential which describes interactions between all atoms [54,55]. This approach significantly reduces the computation cost and allows analyzing large atomic clusters. ReaxFF potential consists of various potential energy functions, including Coulomb and van der Waals interactions, which provide accurate descriptions of bond breaking and bond formation. A full description of these functions can be found in Ref. [54]. Each ReaxFF function is based on an appropriate many-body expansion and is obtained from solving the Schrödinger equation for fixed positions of the nuclei [56].

The ReaxFF method retains nearly the accuracy of quantum mechanical calculations [54,55]. However, it neglects electron-electron correlations. Therefore this method is very promising to simulate the lattice dynamics for the case when electron-electron correlations are screened by photoexcitation of a dense electron-hole plasma.

VO₂ is a strongly correlated oxide and electron correlations play an important role in stabilization of the low- T monoclinic VO₂ lattice. The semiclassical method of MD provides an estimation rather than the actual trajectory of the lattice transformation, where the final structure corresponds to an equilibrium uncorrelated structure of VO₂ which is neither monoclinic nor rutile. Therefore, taking the real “correlated” structure of VO₂ as the input for MD calculations, we obtain the evolution of correlated to uncorrelated VO₂ structure. The method of MD does not use an external “excitation.”

To apply the concept of MD, we assume that the ultrafast photoexcitation produces only screening of electron-electron correlations, while all other physical characteristics of VO₂ remain unchanged.

Upon photoexcitation of VO₂, the lattice transformation within the subpicosecond time scale is considered as an adiabatic process, where the energy exchange with the surroundings is neglected. As the input parameters for the MD calculation we use only the initial temperature and cluster of vanadium and oxygen atoms constructed according to VO₂ lattice parameters. Initial velocities of atoms were set according to the Maxwell-Boltzmann distribution, and the calculation was performed for adiabatic relaxation with a constant number of particles, volume, and total energy of the system.

To model the photoinduced lattice dynamics, the initial lattice parameters of the monoclinic VO₂(M_1) unit cell were taken from experimentally obtained data in Ref. [5]: $a_m = 5.7517$ Å, $b_m = 4.5378$ Å, $c_m = 5.3825$ Å, and the angle between a_m and c_m axes is $\beta_m = 122.646^\circ$. The MD computation was performed for a VO₂(M_1) cluster of 20 217 atoms at temperatures $T = 15$ K and $T = 313$ K. In order to reduce the random component of atomic motion, the main calculations were performed for $T = 15$ K. To estimate the influence of oxygen vacancies on MD, additional calculations were performed for a VO₂(M_1) cluster with 2.5% of vacancy defects randomly distributed inside the lattice. The 2.5% oxygen deficiency is close to the stability limits for the VO₂ structure. To compare MD of monoclinic VO₂(M_1) and rutile VO₂(R), we also calculated MD for a VO₂(R) cluster of 49 152 atoms at temperature $T = 385$ K, slightly above the T_c point. Crystal structure parameters for rutile VO₂(R) were taken from Ref. [6] ($a_r = 4.53$ Å, $b_r = 4.53$ Å, $c_r = 2.869$ Å).

The computational study of adiabatic lattice dynamics reveals significant instability of the VO₂ lattice with monoclinic symmetry, while the rutile phase was found to be relatively stable. Figure 1(a) shows the time evolution of kinetic energy E_{kin} and effective transient temperature T^* for VO₂(M_1) and VO₂(R). The temperature T^* was calculated from kinetic energy through the equation $E_{\text{kin}} = 3/2Nk_B T^*$, where N is the number of atoms and k_B is the Boltzmann constant. A comparison of kinetic energy evolution for monoclinic and rutile phases shows that E_{kin} for VO₂(M_1) increases within 900 fs by two orders of magnitude, from 45 to 2.29×10^3 cal/mole, while for VO₂(R) this change is noticeably less. For VO₂(R) E_{kin} changes from 1.15×10^3 to 1.05×10^3 cal/mole: After a small drop it returns to nearly the same level. The dynamics of VO₂(M_1) is more pronounced, and the increase of the temperature from $T(0 \text{ fs}) = 15$ K to $T(0 \text{ fs}) = 313$ K [Fig. 1(b)] does not noticeably affect the relaxation kinetics, but results in an increase of the final average level of E_{kin} to 2.7×10^3 cal/mole ($T^* = 905$ K).

A significant difference in the relative change of E_{kin} for the correlated low- T monoclinic phase and for the noncorrelated high- T rutile phase was *a priori* expected as the result of photoinduced screening of electron correlations, and eventually reliably confirmed by the ReaxFF-based MD simulation. Thus, a screening of Coulomb repulsion for noncorrelated rutile VO₂ does not provide a considerable change of E_{kin} , while for the correlated low- T monoclinic phase the screening results in

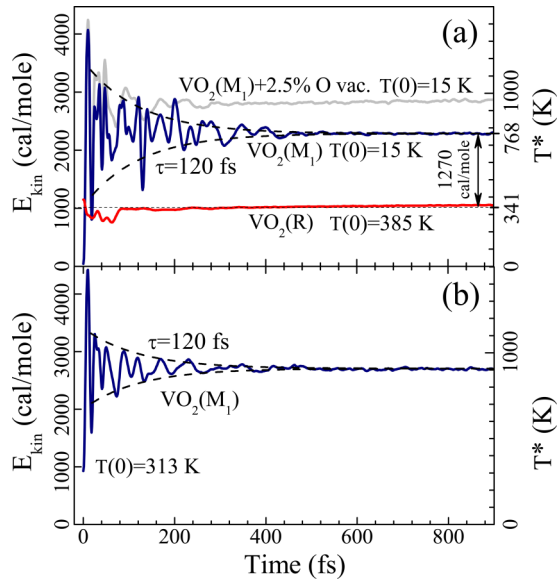


FIG. 1. (a) The time evolution of kinetic energy and effective transient temperature T^* for pure monoclinic VO₂(M₁) and for structure with 2.5% of oxygen vacancies [VO₂(M₁) + 2.5% O vacancy] at $T = 15$ K and for rutile VO₂(R) at $T = 385$ K. (b) Kinetic energy and T^* for VO₂(M₁) at $T = 313$ K. The envelope is shown by dashed lines for VO₂(M₁) at $t > 20$ fs.

an instantaneous rise of kinetic energy followed by lattice instability. Also, this indicates that the electron correlations in the low- T phase are the major factor in stabilizing the VO₂ monoclinic symmetry.

The envelope of $E_{\text{kin}}(t)$ for $t > 20$ fs in Fig. 1 can be approximated by the function $E_0 \pm E_1 \exp(-t/\tau)$, where E_0 and E_1 are fitting constants and τ is a characteristic relaxation time. The transient dynamics of kinetic energy shows near-exponential oscillatory decay with $\tau = 120$ fs. This process is associated with elastic phonon-phonon scattering and randomization of the phase of coherent phonon oscillations. Moreover, this result strongly supports the estimation of characteristic time for the resonant elastic scattering of optical phonons on V-V dimers performed in Ref. [57]. The time $\tau = 120$ fs is comparable to experimentally observed characteristic time of the fastest component of the photoinduced structural transition in VO₂, which ranges from ~ 80 fs to several hundred femtoseconds [39]. Therefore, it is very likely that the elastic phonon-phonon scattering in a highly nonequilibrium environment plays a significant role in the SPT dynamics, triggering the lattice transformation from monoclinic to rutile symmetry on the subpicosecond time scale.

The computation of VO₂(M₁) lattice dynamics at low-temperature $T(0 \text{ fs}) = 15$ K results in an increase of the effective temperature up to $T^* = 768$ K [Fig. 1(a)] which is very close to the Debye temperature of VO₂ ($T_D = 750$ K) [58,59]. This fact indicates a possibility of excitation of all vibration modes in high- T VO₂ [60] and, very likely, it contributes to structural instability of photoexcited low- T phase, even at initial temperature as low as 15 K. On the observed time scale the average kinetic energy approaches to $E_{\text{kin}} = 2.29 \times 10^3$ cal/mole. The difference between this energy and the energy which corresponds to the transition

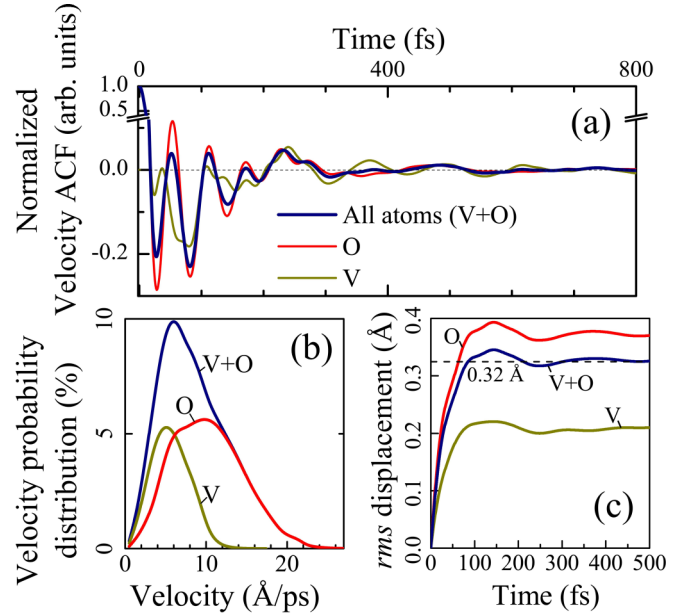


FIG. 2. The computation of molecular dynamics for vanadium (V), oxygen (O), and for all atoms (V + O) of VO₂(M₁) at $T = 15$ K. (a) Velocity autocorrelation function. (b) Velocity probability distribution within 500 fs. (c) rms atomic displacement.

temperature $T_c^* = 341$ K ($E_{\text{kin}} = 1.02 \times 10^3$ cal/mole) is 1.27×10^3 cal/mole. It is noted that this value is very close to the latent heat of the phase transition experimentally obtained by Ryder [58] (1.02×10^3 cal/mole) and by Chandrashekar *et al.* [59] (1.12×10^3 cal/mole). In terms of thermodynamics, this means that the photoinduced screening of electron-electron correlations triggers an exothermic reaction which guarantees the thermally induced phase transition of VO₂, even if the initial temperature of the sample is near absolute zero.

Additional analysis of the VO₂(M₁) cluster with 2.5% of oxygen vacancies shows that the structural defects slightly increase the kinetic energy released during the phase transition [Fig. 1(a)], while the nonequilibrium dynamics remains nearly the same as for pure crystalline VO₂. Therefore, it could be expected that the vacancies facilitate the ultrafast SPT. However, the MD calculations do not consider an influence of defects on the formation of specific localized electronic states which can significantly contribute in SPT dynamics. As a result, the real photoinduced dynamics in VO₂ with high concentration of structural defects can be more complex.

Figures 2(a) and 2(b) show the velocity autocorrelation function (ACF) and velocity probability distribution for vanadium and oxygen atoms, respectively. The velocity ACF shows oscillatory decay within ~ 500 fs. This behavior indicates initial coherent atomic motion, but coherency eventually vanishes in ~ 500 fs. Within this time scale the rms displacement of all atoms [i.e., weighted average rms value for V and O atoms; Fig. 2(c)] shows some oscillatory behavior, approaching the value of 0.32 Å with respect to initial position. While the rms displacement is not, strictly speaking, an order parameter η_c (effective displacement of lattice ions during photoinduced SPT), it compares well with the value of $\eta_c = 0.26$ Å obtained recently by van Veenendaal for ultrafast SPT in VO₂ [37].

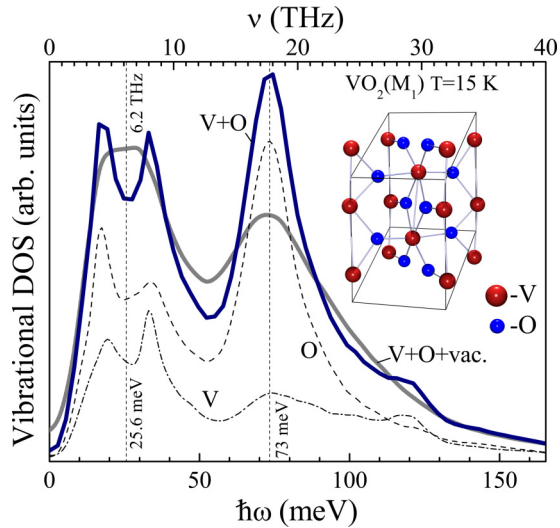


FIG. 3. Vibrational density of states of all atoms (V + O) and only oxygen (O) and vanadium (V) atoms. Calculations are performed for pure $\text{VO}_2(M_1)$ and for $\text{VO}_2(M_1)$ with 2.5% of oxygen vacancies (V + O + vacancy).

Therefore, it is reasonable to expect a correlation between these two values within ~ 500 fs.

The vibrational density of states (DOS) for the $\text{VO}_2(M_1)$ cluster was computed by Fourier transform of the atomic velocities [61]. Figure 3 shows the DOS computed within 1-ps time scale for all atoms and for O and V atoms separately. Additionally, DOS was calculated for the lattice with 2.5% of oxygen vacancies. The presence of structural defects results in smearing of sharp resonance peaks, but the overall spectrum of vibrational DOS remains the same. MD computation clearly shows two broad resonances of optical phonons with maxima at 6.2 THz (25.6 meV) and at 17.7 THz (73 meV). The VO_2 lattice oscillations near 6 THz were observed in several previous studies [32,33,39,43,49,62,63]. The second resonance was clearly observed by Kübler *et al.* in Ref. [32]. Thus, the calculated spectrum of vibrational DOS is fully supported by the experimental time domain and THz spectroscopy data.

III. EXPERIMENT

Several high quality epitaxial and nonepitaxial VO_2 films with substantially different morphology, different thicknesses, domain structure, and in-plane oriented crystallites were synthesized. VO_2 films with thicknesses of 30 nm, 50 nm, 80 nm, and 100 nm were grown by pulsed laser deposition (PLD) technique on amorphous SiO_2 and single crystal Al_2O_3 (C-cut and A-cut sapphire) substrates. An excimer KrF laser with 20-ns pulses of 248-nm wavelength, was used to ablate a rotating metallic vanadium (99.95% purity) target, using ~ 4 J/cm² laser fluence. VO_2 films were grown at 30 mTorr pressure in the PLD chamber, in oxygen and argon atmosphere, with O_2 and Ar flow rates of 20 and 5 std. cm³/min, respectively. The substrate temperature was maintained at 550 °C.

All samples were prepared at identical nominal conditions using the same protocol of PLD growth. Deposition of VO_2 on different substrates provided a variety of desired structures and

morphologies of the material. The VO_2 films' phase, crystallographic orientation, and morphology was determined by x-ray diffraction (Bruker D8 Discover x-ray diffractometer) and atomic force microscopy (AFM, Park Scientific Instruments, Autoprobe CP). Only VO_2 films with the single monoclinic M_1 phase at room temperature were selected for the current study.

The synthesis of VO_2 on single crystal sapphire resulted in epitaxial films and relatively low concentration of structural defects [42,64]. These films experience moderate misfit strain owing to lattice mismatch at the film/substrate interface [65–67]. As determined from the XRD data for $\text{VO}_2/\text{Al}_2\text{O}_3$ (A cut), the film's out-of-plane orientation is with its b_m axis normal to the substrate surface. Additional azimuthal φ scans of the sample were performed to determine the in-plane orientation of VO_2 crystallites. It was found that the film a_m axis is normal to the sapphire c axis [0001]. Therefore, the c_m axis is also in the film plane.

For VO_2 deposited on the (0001) Al_2O_3 (C-cut) substrate, the XRD reflection at $2\theta = 39.8^\circ$ indicated that the $(010)_m$ planes are parallel to the substrate surface. Due to the threefold symmetry of sapphire around the c axis, the deposited VO_2 film is twinned, with orientation of the a_m axis along three equivalent crystallographic directions of the substrate as $[100]_m \parallel [100]_{\text{Al}_2\text{O}_3}$, $[100]_m \parallel [010]_{\text{Al}_2\text{O}_3}$, and $[100]_m \parallel [\bar{1}\bar{1}0]_{\text{Al}_2\text{O}_3}$ [42].

VO_2 films deposited on SiO_2 show only out-of-plane orientation, and are expected to have higher concentration of oxygen vacancies and other structural defects. The strong reflection observed at $2\theta = 27.98^\circ$ for VO_2/SiO_2 indicated that the $(011)_m$ plane is parallel to the substrate.

In the present study, the VO_2 films deposited on Al_2O_3 (C cut) and SiO_2 substrates were used to observe the influence of photoacoustic excitations and structural defects on SPT. The 50-nm-thick $\text{VO}_2/\text{Al}_2\text{O}_3$ (C-cut) film was used to monitor fluence-dependent evolution of SPT on a picosecond time scale in order to reconstruct the thermodynamic potential of VO_2 in its nonequilibrium photoexcited state. The $\text{VO}_2/\text{Al}_2\text{O}_3$ (A-cut) film was used to study the influence of misfit strain and structural anisotropy on SPT dynamics.

A Spectra-Physics Ti:sapphire femtosecond laser system was used as a source to induce and to monitor the phase transition dynamics of VO_2 at room temperature. The system generates light pulses with $\lambda = 800$ nm wavelength and 130-fs duration. Owing to the relatively slow recovery rate of nonepitaxial VO_2/SiO_2 after optical excitation [68,69], to monitor SPT in these films the repetition rate of laser pulses was set to 200 Hz. To study epitaxial $\text{VO}_2/\text{Al}_2\text{O}_3$ films the laser repetition rate was set to 1 kHz. In this work, we performed different pump-probe transient reflection, transmission, and light scattering measurements. Depending on experimental geometry, the wavelengths of pump and probe pulses were $\lambda = 800$ nm or frequency-doubled $\lambda = 400$ nm by a BBO crystal.

The time- and angle-resolved hemispherical elastic light scattering (TARHELs) technique was used to study multiscale dynamics of photoinduced SPT in VO_2 . The scatterometer setup is illustrated in Fig. 4. In all scattering measurements, the pump ($\lambda = 800$ nm) and probe ($\lambda = 400$ nm) pulses are overlapped on the sample surface at normal incidence and

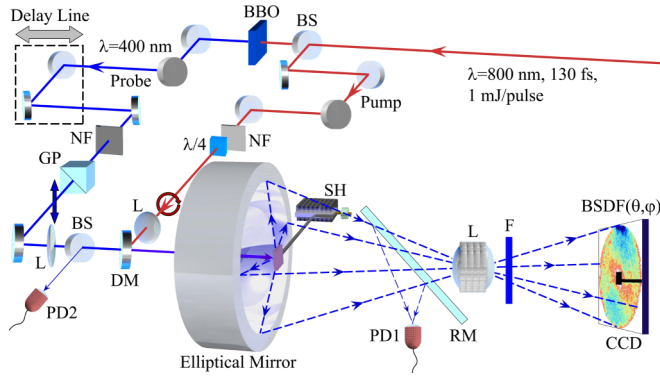


FIG. 4. Experimental setup for ultrafast angle-resolved light scattering measurements within the hemisphere. BS, beam splitter; DM, dichroic mirror; GP, Glan-type polarizer; NF, neutral density filter; F, color filter; L, lens; $\lambda/4$, quarter-wave plate; SH, sample holder; PD1 and PD2, silicon photodetectors; RM, removable mirror.

focused to a spot size of 0.7 mm and 70 μm , respectively. To prevent nonlinear interaction of probe pulse with the sample, its intensity was reduced by several orders of magnitude compared to pump pulse. Probe light was linearly polarized by a Glan-type prism GP. The polarization of pump pulse was set circular by quarter-wave plate $\lambda/4$. A computer-controlled optomechanical delay line was used to set a time delay t between pump and probe pulses with a resolution of 10 fs. Samples were placed at the focal point of the custom-built metallic elliptical mirror with 20-cm diameter aperture. The mirror was used to collect scattered light within the whole hemisphere over the sample surface and to project the image to a 16-bit charge-coupled device (CCD) [70]. Color filter F was used to filter out the pump wavelength light from the recorded image. Obtained scattering patterns were recalculated into indicatrices of bidirectional-scatter-distribution function (BSDF) versus polar θ and azimuthal φ angles or spatial frequency f of the surface. BSDF is the function with close resemblance to surface power spectral density, and it can be used for the surface analysis within “scatter prediction” approach [71]. Two amplified silicon detectors PD1 and PD2 were used to monitor transient total integrated scattering and reflection correspondingly. Detectors are conjugated with a gated data processor.

IV. RESULTS AND DISCUSSION

The light-induced SPT in VO₂ is a complex process which depends on excitation wavelength, fluence, and sample morphology. A laser pulse with fluence above the phase transition threshold ($F_0 \simeq 3 \text{ mJ/cm}^2$) induces ultrafast structural transition, accompanied by a noticeable change of optical and electronic properties of VO₂. Therefore dynamics of the SPT can be tracked by monitoring transient reflectivity $R(t)$, transmittance $\text{Tr}(t)$ or light scattering $I_s(t)$. Figure 5 shows the typical evolution of the ultrafast light scattering signal (inset) upon photoinduced phase transition within ~ 500 fs and also differential reflectivity (main panel) within several nanoseconds for an epitaxial 50-nm VO₂/Al₂O₃(C-cut) film. Rigorous observation of the SPT in different samples by pump-probe optical techniques allows distinguishing several

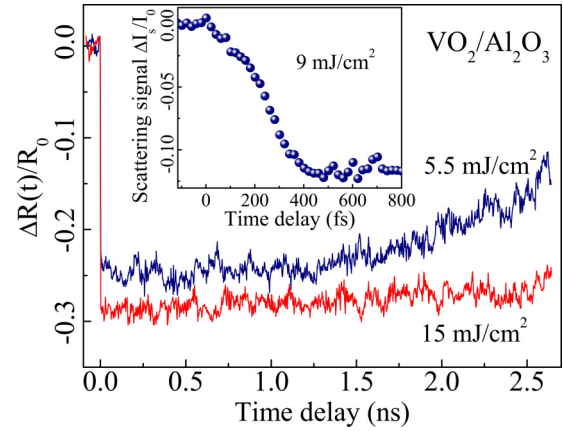


FIG. 5. Evolution of transient differential reflectivity $\Delta R(t)/R_0$ upon photoinduced phase transition of epitaxial 50-nm VO₂/Al₂O₃(C-cut) film at different levels of optical excitation. R_0 is the reflectivity of an unperturbed sample, $\Delta R(t) = R(t) - R_0$. The wavelengths of the optical pump and probe pulses are 400 and 800 nm, respectively. The inset shows transient differential signal $\Delta I_s(t)/I_0$ of light scattering integrated within the hemisphere. I_0 is the scattering signal of the unperturbed sample, $\Delta I_s(t) = I_s(t) - I_0$.

characteristic time scales for qualitatively different transient dynamics. These are time scales (i) up to ~ 500 fs, (ii) between 500 fs and ~ 40 ps [72], and (iii) above ~ 40 ps. In the next sections, we discuss the SPT and specific optical response for each time scale. We will address first the dynamics (iii) in Sec. IV A, then (i) in Secs. IV B and IV C, and finally (ii) in Sec. IV D.

A. The role of photoacoustic excitations in phase transition dynamics on nanosecond time scale

Using VO₂ films with different thicknesses and morphologies, it is possible to enhance and monitor specific nonequilibrium processes. The transient reflection and transmission both provide essentially the same information about the photoinduced phase transition in VO₂. For 50-nm VO₂/Al₂O₃ film, the differential signal of transient reflection is much stronger as compared to the transmission. Therefore, to obtain higher signal-to-noise ratio, the NLO dynamics for this sample was studied in reflection geometry. On the other hand, for thicker, 100-nm VO₂/SiO₂ film, the interference effects introduced some artifacts into the reflection signal. Therefore, for this sample reliable information about the phase transition dynamics was obtained from transmission measurements.

Figures 5 and 6 show a significant difference between two NLO processes for the nanosecond time scale, for 50-nm thick epitaxial VO₂/Al₂O₃ and for non-epitaxial 100-nm thick VO₂/SiO₂ films. It was found that the VO₂/Al₂O₃ film switches into the metallic phase rapidly without noticeable posterior dynamics at $F = 15 \text{ mJ/cm}^2$. The recovery process back to the insulating phase starts at ~ 1.3 ns, as the laser fluence drops to 5.5 mJ/cm^2 . The photoexcitation of 100-nm thick VO₂/SiO₂ film shows more complex dynamics [Fig. 6(a)].

A similar behavior of the optical signal for VO₂/SiO₂ and VO₂/Al₂O₃ films was found within several picoseconds

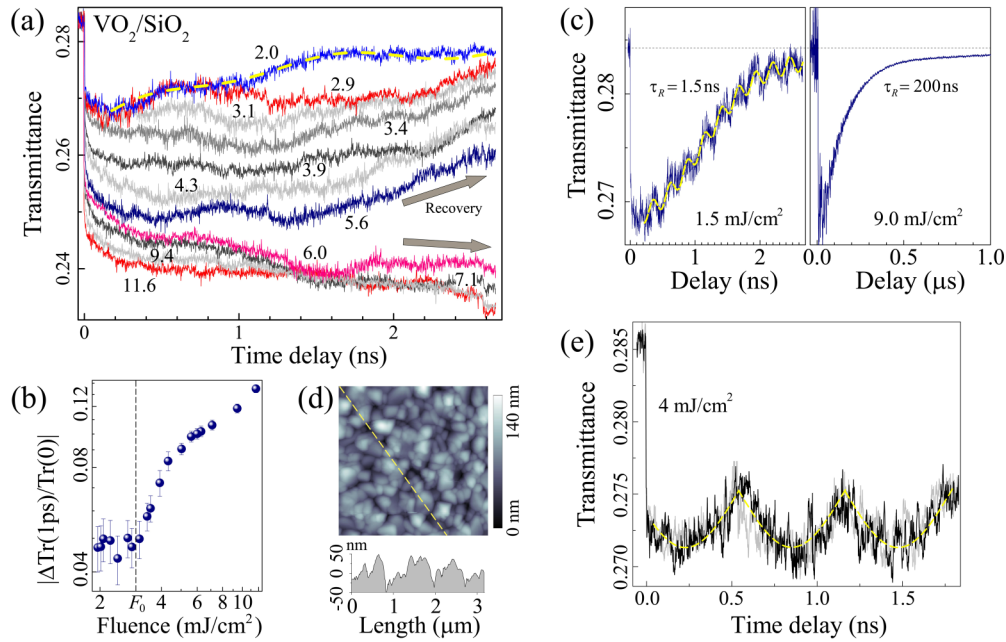


FIG. 6. Nonlinear optical dynamics of 100-nm VO_2/SiO_2 film. (a) Transient transmittance of the film upon optical excitation. Numbers specify the laser pump fluence in mJ/cm^2 . Gray arrows show two distinctly different directions of relaxation kinetics for the fluence below and above $6 \text{ mJ}/\text{cm}^2$. The dashed curve is a fit using Eq. (1). (b) Magnitude of relative change $|\Delta\text{Tr}(1 \text{ ps})/\text{Tr}(0)|$ of transmittance at 1-ps delay, where $\Delta\text{Tr}(1 \text{ ps}) = \text{Tr}(1 \text{ ps}) - \text{Tr}(0)$. (c) Transient transmittance showing recovery of VO_2/SiO_2 film into insulating phase at different levels of optical excitation. The oscillatory part of the signal at $F = 1.5 \text{ mJ}/\text{cm}^2$ fitted (dashed curve) by Eq. (1). The signal on the right panel was obtained by using a continuous wave laser source. (d) AFM topography of the $2.6 \times 2.6 \mu\text{m}^2$ area. The lower panel shows a cross section of the AFM image corresponding to the dashed line in the image. (e) Two consecutive measurements of transient transmittance within the same area of the sample, confirming a pronounced oscillatory behavior. Dashed curves show the fit to equation $A_0 - A_2 |\sin(2\pi\nu t + \varphi_0)|$.

after optical excitation. The NLO response within 1 ps for thinner (50 nm) $\text{VO}_2/\text{Al}_2\text{O}_3$ film was reliably observed only at $F \geq 3 \text{ mJ}/\text{cm}^2$, while at lower fluence the increased noise significantly affected the measurement accuracy. For 100-nm-thick VO_2/SiO_2 film the NLO response was much stronger. By plotting the NLO signal at 1-ps delay versus pump fluence for this sample, it was possible to derive accurately the threshold fluence F_0 , required to initiate the ultrafast SPT in VO_2 material [49]. Thus, Fig. 6(b) shows the normalized instantaneous change of transmittance $|\Delta\text{Tr}(1 \text{ ps})/\text{Tr}(0)|$, where the increasing optical excitation contributes to the rise of the optical transmission starting from a fluence of $3 \text{ mJ}/\text{cm}^2$. This specific optical response indicates a qualitative change in NLO dynamics of VO_2 . As shown by O’Callahan *et al.* [49], the threshold F_0 can vary for different VO_2 samples within a short range: from 2 to $6 \text{ mJ}/\text{cm}^2$ and, according to the literature [31–33,50,52,73], the fluence of $3 \text{ mJ}/\text{cm}^2$ compares well with the threshold values for the ultrafast phase transition in VO_2 . Therefore, in this study, we assume that the observed qualitative change of the NLO signal at fluence $F_0 = 3 \text{ mJ}/\text{cm}^2$ is related to the threshold of the subpicosecond SPT of VO_2 .

At $F < 3 \text{ mJ}/\text{cm}^2$ the subpicosecond NLO signal $|\Delta\text{Tr}(1 \text{ ps})/\text{Tr}(0)|$ is nearly constant. Presumably, in this case the NLO response is related to photogeneration of dense electron-hole plasma in the film. However, on the longer (picosecond) time scale the transient transmission shows a decrease within the first 200 ps [Fig. 6(a)], associated with the SPT.

Figure 6(a) shows a striking difference in the pathways of phase transition dynamics for VO_2/SiO_2 below and above the $F = 6 \text{ mJ}/\text{cm}^2$ pump level. At lower excitation, the system recovers back into the initial insulating phase within several nanoseconds, while at higher excitation the recovery process does not start on the observed time scale, and the film is continuously switching into its metallic state. This transition is associated with nucleation and growth of metallic phase inside of photoexcited monoclinic VO_2 . Moreover, above $F = 6 \text{ mJ}/\text{cm}^2$ the total SPT dynamics does not depend much on the excitation level, and the full recovery of the system occurs on the microsecond time scale, as shown in Fig. 6(c) for the fluence $9 \text{ mJ}/\text{cm}^2$.

Figures 6(a) and 6(c) show that the increase in the excitation level above $6 \text{ mJ}/\text{cm}^2$ to $9 \text{ mJ}/\text{cm}^2$ increases the characteristic recovery time τ_R by more than two orders of magnitude: from $\tau_R = 1.5 \text{ ns}$ ($F = 1.5 \text{ mJ}/\text{cm}^2$) to $\tau_R = 200 \text{ ns}$ ($F = 9 \text{ mJ}/\text{cm}^2$). This evidences the major contribution of heat to the SPT on a nanosecond time scale at pump fluence above $6 \text{ mJ}/\text{cm}^2$: The heat increases the film temperature above T_c and, therefore, stabilizes the metallic phase. As a result, the recovery time depends only on heat sink into the substrate within several microseconds. However, it is very likely that at laser excitation below $6 \text{ mJ}/\text{cm}^2$ the average temperature of the film does not reach T_c point and the system recovers rapidly, within several nanoseconds. We note that the repetition rate of the laser pulses was reduced to 200 Hz for all measurements of nonepitaxial VO_2/SiO_2 film. This rate was sufficient to provide complete heat sink to the substrate and to prevent

any possible accumulation of the heat in the film during the repetitive excitation of the sample.

The NLO dynamics of VO₂/SiO₂ shows the complex behavior. For $F = 1.5 \text{ mJ/cm}^2$ [Fig. 6(c)] it was possible to resolve oscillations with frequency $\nu = 4 \times 10^9 \text{ Hz}$ and with impulse response:

$$\text{Tr}(t) \approx A_0 + A_1[1 - \exp(-t/\tau_R)] + A_2 \sin(2\pi\nu t + \varphi_0), \quad (1)$$

where A_0 , A_1 , and A_2 and time τ_R are fitting constants and φ_0 is the initial phase. Taking into account relatively low frequency of observed oscillations, the oscillatory signal was assigned to photoacoustic material response.

The speed of the acoustic wave propagating across the film of thickness d can be estimated using the following equation [74–76]: $v = 4dv$. For $d = 100 \text{ nm}$ and $\nu = 4 \times 10^9 \text{ Hz}$, one obtains the speed $v = 1600 \text{ m/s}$. This value is less than half the speed of sound in single-crystal VO₂ ($v = 4000 \text{ m/s}$) [77]. Such a large difference can be related to an amorphous structural component of the film as well as to possible change of mechanical properties of VO₂ in its photoexcited nonequilibrium state.

At the fluence $F = 2.0 \text{ mJ/cm}^2$ the frequency of oscillations decreases to $\nu = 7 \times 10^8 \text{ Hz}$ [Fig. 6(a)]. This low-frequency oscillatory response is difficult to associate with acoustic waves propagating in a normal direction to the film surface. Additional contribution into oscillatory dynamics can be produced by acoustic waves propagating in the lateral direction. According to AFM data [Fig. 6(d)], the grain size in the film ranges from $0.2 \mu\text{m}$ to $\sim 1 \mu\text{m}$. Rough estimation shows that the acoustic wave with $\nu = 7 \times 10^8 \text{ Hz}$ can be excited within a large grain of size $1\text{--}2 \mu\text{m}$.

In some areas of the film we observed a strong oscillatory signal with $\nu = 8 \times 10^8 \text{ Hz}$ and with 2% modulation of the sample transmittance, as shown in Fig. 6(e). The signal is proportional to $A_0 - A_2|\sin(2\pi\nu t + \varphi_0)|$. This distinct behavior may be assigned to photoacoustically driven ferroelastic SPT, where a standing acoustic wave modulates the strain field in the large VO₂ grain.

Obtained experimental data allows describing the light-induced SPT of VO₂ in terms of the free energy difference ΔG between insulating and metallic phases. The potential barrier ΔG is a function of temperature T_0 at the phase boundary and actual temperature T , molecular latent heat q , number of molecules N , pressure p , and specific surface energy σ , and can be expressed as [78]

$$\Delta G = -(Nq/T)\Delta T - Nk_B T \ln(p/p_0) + N\Delta\mu + \sigma\Delta s, \quad (2)$$

where $\Delta T = T - T_0$, Δs is the surface area of nucleating grain, domain or cluster, $\Delta\mu$ is the chemical potential related to the difference in the bonding of VO₂ molecules for metallic and insulating phases; p_0 is the equilibrium pressure at the thermodynamical phase boundary.

Heat and strain significantly contribute to SPT on the nanosecond time scale via changing ΔG . Equation (2) provides a straightforward explanation of this dynamics. While the first term of Eq. (2) is related to the conventional contribution of heat, the second term is related to the photoinduced pressure

and strain in the film. The photoexcitation decreases the binding energy difference $N\Delta\mu$, increases lattice temperature via electron-phonon and phonon-phonon scattering, generates acoustic phonons and, as a result, alters ΔG producing the SPT on the nanosecond time scale.

Since VO₂/SiO₂ is a nonepitaxial film and is expected to have relatively high acoustic impedance and high thermal boundary resistance [68], generated acoustic phonons should be confined inside the film and do not propagate into the substrate on the monitored nanosecond time scale. As a result, these phonons provide significant contribution into ferroelastic SPT. In contrast to VO₂/SiO₂, for epitaxial VO₂/Al₂O₃ films the photoacoustic response was not observed clearly due to lower acoustic impedance (see Fig. 5). Owing to the epitaxial nature of VO₂/Al₂O₃, phonons leave the film volume rapidly without noticeable acoustic modulation of the optical properties. Nevertheless, a recent observation of phonon dynamics in an epitaxial VO₂/Al₂O₃ film by Abreu *et al.* [79] shows that the lowering of the sample temperature increases the signal-to-noise ratio and provides reliable detection of acoustic phonons.

B. Grain-size-dependent subpicosecond phase transition dynamics in the presence of anisotropic internal misfit strain

As shown above (see Fig. 6) the strain field produced by photoacoustic wave in VO₂ plays an essential role in the light-induced SPT on the nanosecond time scale. According to recent studies of ultrafast light scattering [80,81], the influence of internal strain on the subpicosecond SPT dynamics of VO₂ is also significant. In order to obtain new information about how internal strain affects the femtosecond SPT, we used an 80-nm-thick epitaxial VO₂/Al₂O₃(A-cut) film with anisotropic misfit strain.

Since the VO₂ film was deposited in its rutile phase, because of the growth temperature employed, the magnitude of misfit strain in the film can be obtained by considering the lattice mismatch between VO₂(*R*) and sapphire Al₂O₃(A-cut) substrate. The sapphire A plane represents the cross section of the unit cell along [0001] and $[\bar{1}100]$ directions with respective values c_{saph} and $\sqrt{3}a_{\text{saph}}$, where $c_{\text{saph}} = 12.993 \text{ \AA}$ and $a_{\text{saph}} = 4.759 \text{ \AA}$ [82]. These distances are large in comparison with the VO₂(*R*) lattice parameters, but accommodation occurs by multiples of the a_r and c_r parameters. Corresponding to the substrate [0001] direction it is noted that $c_{\text{saph}} \approx 3a_r$, with a lattice mismatch of approximately -4.4% . Corresponding to the substrate $[\bar{1}100]$ direction, $\sqrt{3}a_{\text{saph}} \approx 3c_r$ with a lattice mismatch of -4.2% . Both of these values imply that as the VO₂(*R*) film grows on the A-cut sapphire substrate, it will be compressed in all directions along its surface. As the film is cooled to room temperature, strains will change, because of (i) the phase transformation and (ii) film-substrate thermal expansion mismatch. However, consideration of the VO₂(*M*₁) lattice parameters and their orientation on the sapphire A surface shows that the relatively large strain values calculated above will be largely maintained.

To observe the influence of misfit strain on femtosecond SPT as a function of surface spatial frequency, we performed TARHELS measurements. These measurements provide spatial resolution of phase transition dynamics in differently

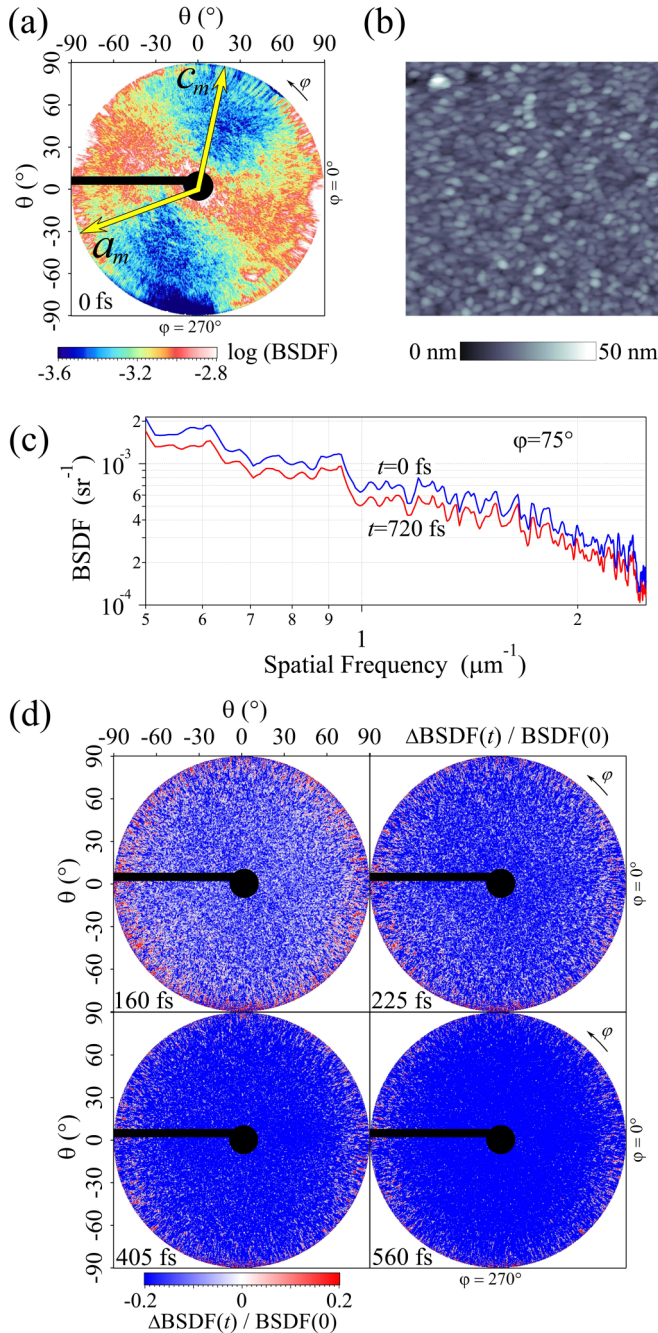


FIG. 7. (a) Scattering indicatrix for unexcited $\text{VO}_2/\text{Al}_2\text{O}_3$ (A-cut) film. Arrows show the orientation of a_m and c_m axes of $\text{VO}_2(M_1)$. (b) $5 \times 5 \mu\text{m}^2$ AFM topography of $\text{VO}_2/\text{Al}_2\text{O}_3$ (A-cut) film. The average lateral size of grains is 175 nm and rms surface roughness is 4 nm. (c) BSDF(f) cross sections at $\varphi = 75^\circ$ at $t = 0$ fs and at $t = 720$ fs after photoexcitation; $F = 12 \text{ mJ}/\text{cm}^2$. (d) Transient change $\Delta\text{BSDF}(t)/\text{BSDF}(0)$ of the scattering signal upon light-induced phase transition at $F = 12 \text{ mJ}/\text{cm}^2$, where $\Delta\text{BSDF}(t) = \text{BSDF}(t) - \text{BSDF}(0)$.

oriented groups of domains, grains, and clusters [71]. To avoid experimental uncertainty owing to polarization-dependent excitation of VO_2 , we used a circularly polarized pump pulse.

The BSDF indicatrix of hemispherical light scattering by $\text{VO}_2/\text{Al}_2\text{O}_3$ (A-cut) film is shown in Fig. 7(a). The anisotropy of the scattering pattern is caused by the texture of the epitaxial

film [Fig. 7(b)] which is highly influenced by the single-crystal substrate. The photoinduced SPT at $F = 12 \text{ mJ}/\text{cm}^2$ results in uniform decrease of light scattering intensity for all spatial frequencies. The cross sections of the scattering indicatrix at delay time $t = 0$ fs and $t = 720$ fs [Fig. 7(c)] show that the profile of BSDF distribution versus spatial frequency f remains unchanged during the SPT. Moreover, the relative transient change of the scattering signal $\Delta\text{BSDF}(t)/\text{BSDF}(0)$ [Fig. 7(d)] does not show noticeable angular dependence or anisotropy. Thus, despite the epitaxial nature of the film, the excitation of the film at laser fluence $F = 12 \text{ mJ}/\text{cm}^2$ produces simultaneous SPT with nearly the same rate in all VO_2 grains/domains with different spatial frequencies. These data show uniform and isotropic SPT at this level of optical excitation. Nevertheless, it was found that the SPT dynamics changes dramatically and becomes essentially anisotropic when the excitation reduces to the levels close to the threshold F_0 .

To enhance the influence of anisotropic misfit strain on SPT dynamics in VO_2 grains/domains with different spatial frequencies, the pump fluence was set near the threshold F_0 , at $F = 7 \text{ mJ}/\text{cm}^2$. As shown previously [32,33,43,63], the photoexcitation of VO_2 with relatively low fluence results in activation of coherent phonon mode at ~ 6 THz. This allows us to observe clearly the influence of film morphology on amplitude and evolution of these oscillations.

Transient change of the scattering signal $\Delta\text{BSDF}(t)/\text{BSDF}(0)$ obtained for the same $\text{VO}_2/\text{Al}_2\text{O}_3$ (A-cut) film shows strong oscillatory behavior [Fig. 8(a)] associated with photoexcitation of active Raman modes in monoclinic VO_2 due to stretching and tilting of V-V dimers [32,33,43,62,63]. In the central part of scattering indicatrix, the amplitude of oscillations is relatively high, but it decreases at larger polar angles and the transient signal decays rapidly. Due to epitaxial orientation of the film, oscillatory response of grains/domains contributes to symmetric diffraction pattern outlined by dashed rhomb in the center of scattering indicatrix.

The cross section of the $\Delta\text{BSDF}(t)/\text{BSDF}(0)$ indicatrix at two azimuthal directions $\varphi = 215^\circ$ and $\varphi = 0^\circ$ [Fig. 8(b)] reveals anisotropy in the evolution of coherent lattice oscillations which accompany the SPT. The dashed line in the figures separates two mainly different areas for the SPT process. Taking into account the essentially nonlinear dynamics of photoexcited VO_2 , the dashed line defines a set of time points when the character of structural dynamics changes qualitatively. For VO_2 structures with higher spatial frequencies the SPT occurs faster, while for structures with $f \lesssim 1.95 \mu\text{m}^{-1}$ at $\varphi = 215^\circ$ and $f \lesssim 1.2 \mu\text{m}^{-1}$ at $\varphi = 0^\circ$ a monotonic phase transformation does not start on the monitored time scale. This behavior evidences the size-dependent and anisotropic SPT dynamics, which rate depends on size and orientation of VO_2 grains/domains in the film.

The oscillation of $\Delta\text{BSDF}(t)/\text{BSDF}(0)$ for larger crystallites is anharmonic and contains several oscillatory modes [see $f = 1.0 \mu\text{m}^{-1}$ in Fig. 8(c)]. However, for smaller grains [see $f \geq 1.5 \mu\text{m}^{-1}$ in Fig. 8(c)] the oscillations become harmonic. The Fourier transform of the oscillatory component for the scattering signal at $f = 2.3 \mu\text{m}^{-1}$ shows a single frequency centered at $\nu_0 = 6.1$ THz [Fig. 9(a)], while for lower spatial frequency $f = 1.0 \mu\text{m}^{-1}$ the Fourier spectrum is more complex.

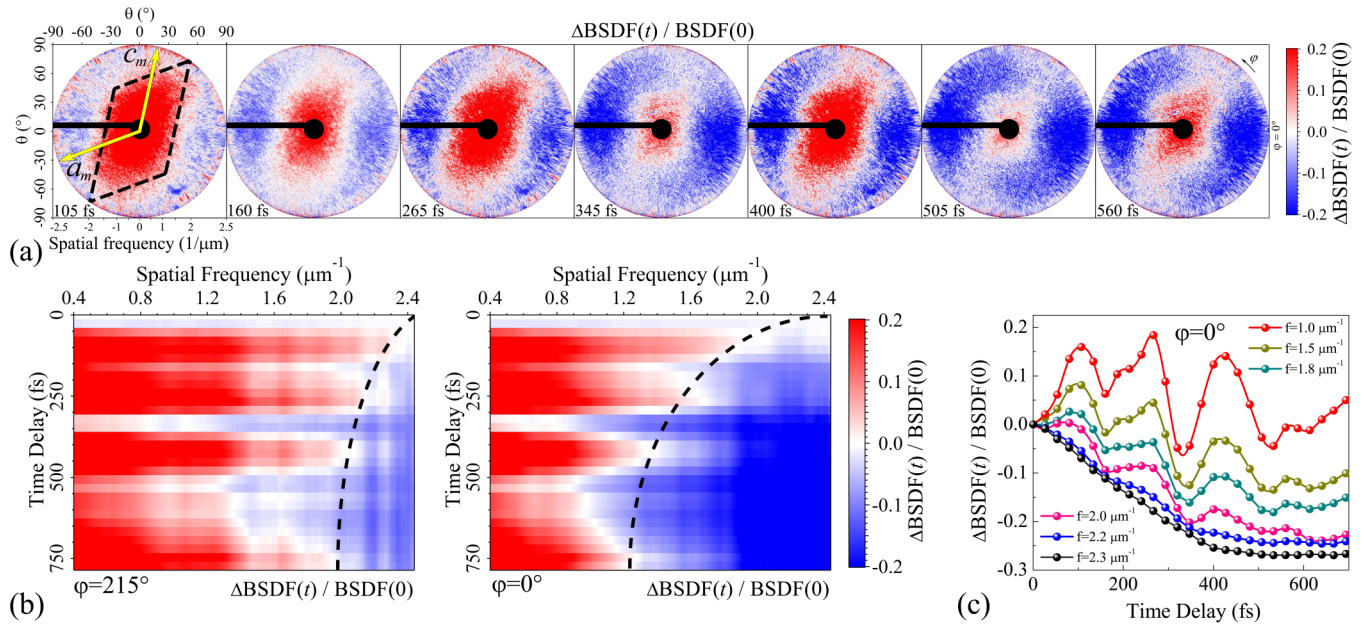


FIG. 8. (a) Transient change $\Delta\text{BSDF}(t)/\text{BSDF}(0)$ of the scattering signal upon light-induced SPT in VO₂/Al₂O₃(A-cut) film; $F = 7 \text{ mJ/cm}^2$. Arrows show the orientation of a_m and c_m axes of VO₂(M_1). Dashed rhomb identifies the oscillatory area of scattering indicatrix. (b) Time-dependent cross sections of the data mapped in (a) at $\varphi = 215^\circ$ and $\varphi = 0^\circ$ versus spatial frequency of surface relief. (c) The cross sections of the data mapped in (b) at $\varphi = 0^\circ$ shows gradual change of oscillatory dynamics versus spatial frequency.

The strong dependence of $\Delta\text{BSDF}(t)/\text{BSDF}(0)$ oscillations versus spatial frequency is attributed to the influence of the misfit strain on thermodynamic potential Φ of photoexcited VO₂. The detailed description of this potential will be given in Sec. IV D. Different strain in VO₂ grains/domains of different size and orientation alters Φ as shown in Fig. 9(b). As a result, the same level of photoexcitation switches these grains/domains into different excited states. In consequence, nonequilibrium dynamics of VO₂ becomes grain-size dependent.

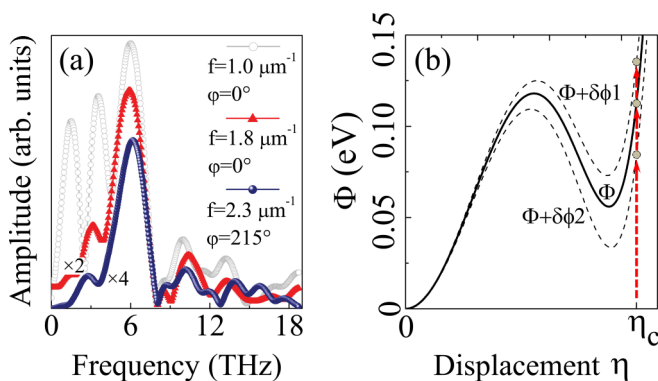


FIG. 9. (a) The Fourier transform of the oscillatory component in the scattering signal for different spatial frequencies. (b) The thermodynamic potential of photoexcited VO₂. Φ is altered by internal strain in the film. Strain contributes in additional positive $\delta\phi_1$ or negative $\delta\phi_2$ component of the potential Φ . Dashed arrows indicate the initial energy of the VO₂ system right after photoexcitation. Here the same level of photoexcitation switches the grains/domains with different thermodynamic potential into different excited states.

It is important to note that at certain scattering angles we were able to resolve oscillations with nearly doubled frequency $\sim 2\nu_0$. Figure 10(a) shows TARHELDS data obtained at $F = 6 \text{ mJ/cm}^2$, at azimuthal direction $\varphi = 250^\circ$, for the same VO₂/Al₂O₃(A-cut) film within $f = 1.8\text{--}2.5 \mu\text{m}^{-1}$. The observed oscillations are localized at certain spatial frequencies and represent nonequilibrium dynamics of certain groups of VO₂ grains. The cross sections of Fig. 10(a) at different spatial frequencies [upper panel of Fig. 10(b) show noticeable oscillatory behavior of the transient signal at $f = 2.12, 2.24, 2.264,$ and $2.46 \mu\text{m}^{-1}$. The lower panel of Fig. 10(b) shows the oscillating part of the signal at $f = 2.46 \mu\text{m}^{-1}$, which can be approximated by the function $A_0 \sin(2\pi\nu t + \varphi_0)$ with $\nu = 11.2 \text{ THz}$. The obtained frequency of 11.2 THz is nearly doubled frequency of the active Raman mode shown in Fig. 9(a). We note that similar oscillations with the frequency $\sim 2\nu_0$ were previously resolved by multiterahertz spectroscopy [33] (12 THz) and by transient reflectivity technique [43] (10 THz).

C. Subpicosecond phase transition in the presence of structural defects

The influence of structural inhomogeneities on transient optical properties was observed for 30-nm-thick nonepitaxial polycrystalline VO₂/SiO₂ film. In contrast to epitaxial VO₂/Al₂O₃(A-cut) film, for VO₂/SiO₂ the oscillations of scattering signal were not resolved. It is very likely that the oscillatory signal is suppressed owing to fluctuation of the initial phase of lattice oscillation in different grains and domains, because of significant randomness in orientation and distribution of VO₂ grains on the surface, as well as the relatively high concentration of structural defects in the nonepitaxial film. At a laser excitation well above the transition

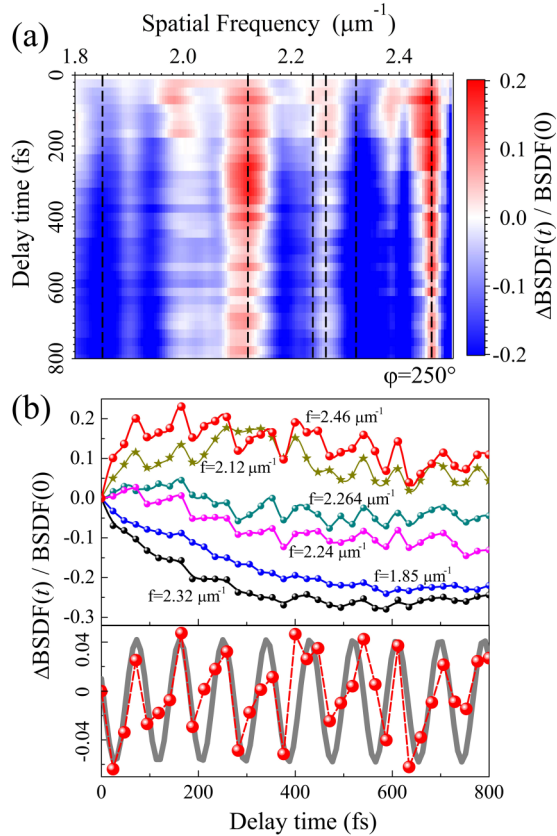


FIG. 10. (a) Transient change $\Delta\text{BSDF}(t)/\text{BSDF}(0)$ of the scattering signal at $\varphi = 250^\circ$ versus spatial frequency of surface relief; $F = 6 \text{ mJ/cm}^2$. (b) (Upper panel) The cross sections of the data mapped in (a) along the time axis marked by dashed lines. (Lower panel) The oscillatory part of $\Delta\text{BSDF}(t)/\text{BSDF}(0)$ obtained by high-pass filtering of the signal at $f = 2.46 \mu\text{m}^{-1}$ (circles). Solid line is the fit to equation $A_0 \sin(2\pi \nu t + \varphi_0)$ with $\nu = 11.2$ THz.

threshold ($F = 15 \text{ mJ/cm}^2$) the scattering signal shows the monotonic rise at $\theta > 70^\circ$ ($f > 2.35 \mu\text{m}^{-1}$) [Figs. 11(a) and 11(b)]. We note that a similar rise of the signal was observed also for epitaxial $\text{VO}_2/\text{Al}_2\text{O}_3$ (A-cut) film [Fig. 7(d)], however, with much lower relative intensity. This behavior is different from the dynamics at lower optical excitation shown in Figs. 8 and 10, and is not related to coherent excitation of optical phonons. As will be shown below, this signal originates from growing optical inhomogeneity in the film.

Taking into account the evolution of the dielectric constant during the IMT from $\varepsilon_i \simeq 7.4 + i5.5$ to $\varepsilon_m \simeq 4.7 + i5.46$ for probe wavelength $\lambda = 400 \text{ nm}$ [83], the scattering cross section of VO_2 should decrease by $\sim 35\%$. This estimation is consistent with $\sim 20\%$ drop of the scattering signal in Fig. 7(d). We note that the optical constants significantly depend on film morphology and concentration of structural defects, and the scattering signal can decrease by a low percentage only. Nevertheless, at excitation levels well above the threshold F_0 , light scattering cannot increase for pure VO_2 and does not show any signature of “transition opalescence” on the subpicosecond time scale, as shown in Refs. [80,84]. However, Fig. 11(b) and the cross sections [Figs. 11(c) and 11(d)] of the scattering indicatrix [Fig. 11(a)] at different time delays show the rise

of the scattering signal above $f = 2.35 \mu\text{m}^{-1}$ ($\theta = 70^\circ$). This behavior can be interpreted as a consequence of increased local optical inhomogeneity in the film, and cannot be assigned to the uniform change of dielectric constant as VO_2 switches from an insulator to metal.

The transient optical inhomogeneity can originate from several major factors: from structural defects of vanadium dioxide and inhomogeneous nucleation of VO_2 sites or from film twinning and geometrical reconstruction of the surface. As shown above [Figs. 7(c) and 7(d)] and in Refs. [80,84], the ultrashort light pulse induces uniform SPT in all VO_2 grains of the thin film and does not modify the surface morphology on the picosecond time scale. Therefore, it is proposed that the most probable origin for the transient increase of scattering signal at the relatively high optical excitation of $F = 15 \text{ mJ/cm}^2$ is the presence of structural defects (presumably oxygen vacancies) in smaller grains with spatial frequencies $f > 2.35 \mu\text{m}^{-1}$.

The nonepitaxial growth of VO_2 on SiO_2 substrate results in a quite disordered structure with numerous oxygen vacancies and other pointlike defects. The concentration of structural defects is higher in the smallest grains of the film [86], and it is very likely that the grains with $f > 2.35 \mu\text{m}^{-1}$ also contain inclusions of VO_x ($1 \leq x \leq 2.5$) oxides [87], other than VO_2 . Thus, VO_2 would undergo the phase transition upon light illumination, while VO_x would remain in the same phase or show different nonlinear optical response as compared to VO_2 . As a result, the system disorder rapidly increases as the VO_2 grains with high concentration of structural defects are switching into the metallic phase.

The MD calculations show that the presence of oxygen vacancies does not noticeably alter the kinetics of SPT [Fig. 1(a)]. This is consistent with experimental data obtained for nonepitaxial VO_2/SiO_2 film with higher structural disorder (Fig. 11), as compared to epitaxial $\text{VO}_2/\text{Al}_2\text{O}_3$ (Fig. 7). Thus, the complete phase transition in VO_2/SiO_2 occurs within the same time scale of ~ 500 fs, as in the case of $\text{VO}_2/\text{Al}_2\text{O}_3$. The phase transition rate within the full monitored range of spatial frequencies of the VO_2/SiO_2 film was found to be nearly the same. However, these films, in contrast to epitaxial films, contain highly disordered structures with $f > 2.35 \mu\text{m}^{-1}$, where the transient signal rises up and has significantly increased noise [Fig. 11(d)]. It is very likely that this noticeable noise component is a signature of alteration of thermodynamic potential Φ and SPT trajectories by structural defects in the smallest VO_2 grains with embedded VO_x sites.

D. Picosecond lattice relaxation and thermodynamic potential

In this section, we discuss the nonequilibrium dynamics on a ~ 40 -ps time scale and perform quantitative reconstruction of the VO_2 thermodynamic potential versus photoexcitation level. For this study we used an epitaxial 50-nm $\text{VO}_2/\text{Al}_2\text{O}_3$ (C-cut) film which absorbs 75% of incident radiation and is sufficiently thin for uniform photoexcitation. Figure 12(a) shows typical transient reflectivities of the film at three different excitation levels: 4 mJ/cm^2 , 6 mJ/cm^2 , and 27 mJ/cm^2 . The inset shows an AFM image of the sample surface, which is more uniform than the VO_2/SiO_2 sample [Fig. 6(d)]. The observed NLO response has two

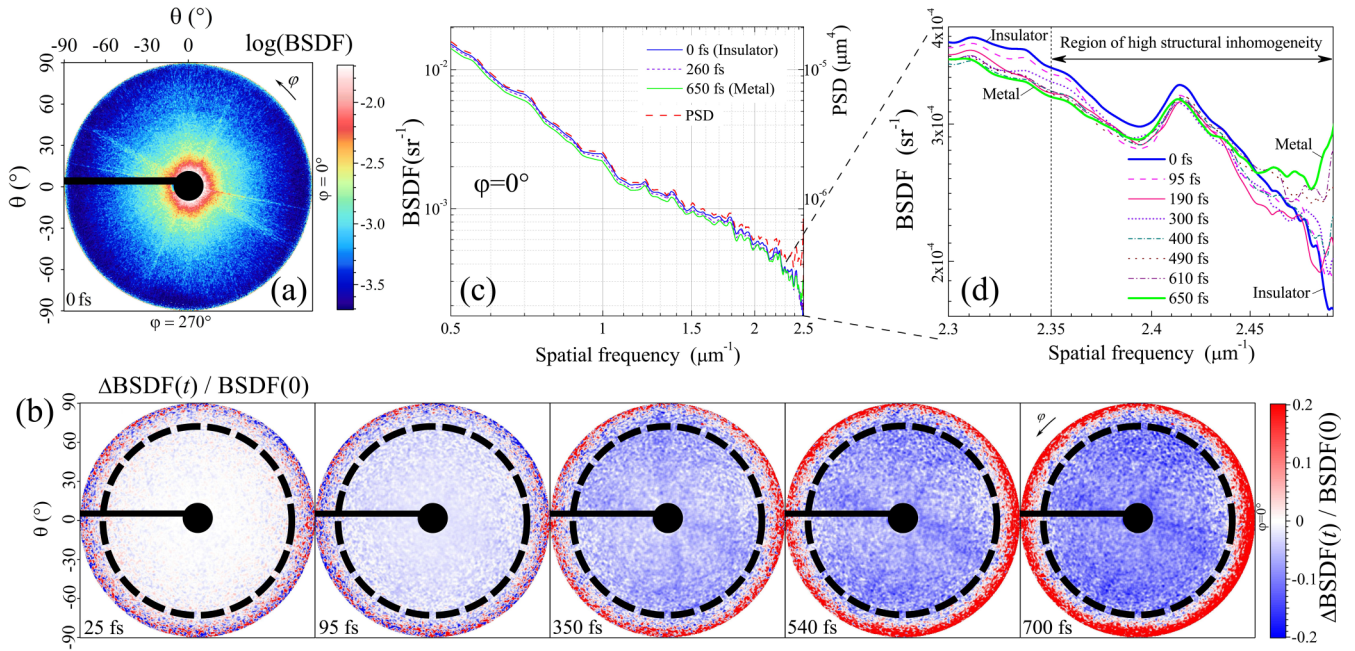


FIG. 11. Ultrafast light scattering by VO₂/SiO₂ at $F = 15 \text{ mJ/cm}^2$. (a) $\log(\text{BSDF})$ indicatrix of the unperturbed sample. (b) Relative change $\Delta\text{BSDF}(t)/\text{BSDF}(0)$ of the scattering signal upon light-induced SPT. Dashed circle separates two regions of different nonlinearity. (c) BSDF and power spectral density (PSD) of the surface obtained by the cross sections of scattering indicatrix at $\varphi = 0^\circ$. PSD was calculated using Elson's theory [85]. (d) Same as (c) for $f = 2.3\text{--}2.5 \mu\text{m}^{-1}$.

distinctive components: instantaneous change of reflectivity within ~ 500 fs and posterior evolution on picosecond time scale. While these two components were observed previously in numerous studies [31,43,50,88], most of the attention has centered so far in the femtosecond response of VO₂. Both components of the NLO signal are related to light-induced phase transition in VO₂ grains, domains, and/or clusters. We also found that the slower (picosecond) component completely vanishes when the laser fluence exceeds $\sim 30 \text{ mJ/cm}^2$. This result agrees with data obtained in Ref. [43].

Taking into account observed NLO dynamics at different levels of optical excitation, we assume that at relatively low laser fluence, much below 30 mJ/cm^2 , not all VO₂ sites (i.e., domains, grains or clusters) are switched into the complete metallic rutile phase within ~ 500 fs. However, their number increases with the pump level. As a result, the relative change of reflection [Fig. 12(a)] or transmission [Figs. 6(a) and 6(b)] also increases with the pump fluence. The rest of the VO₂ sites, which are not switched by light within ~ 500 fs are still in monoclinic but nonequilibrium excited state. These sites can undergo the SPT on longer time scales, where the first-order transition is mainly triggered by electron-phonon and phonon-phonon scattering processes. These processes contribute into nucleation and growth of new rutile phase [57].

The slower (picosecond) nonequilibrium dynamics of VO₂ within ~ 40 ps depends on the laser excitation level. However, we did not find a noticeable dependence of the relaxation rate versus film thickness for different samples, as well as we did not detect oscillations of optical signal which could be assigned to acoustic phonon contribution on this time scale. In Ref. [72], Brady *et al.* also found that the phase transition dynamics within a 40.5 ± 2 -ps time scale is independent on sample morphology.

The structural transformation within several picoseconds involves electron-phonon and anharmonic phonon-phonon scattering processes which allow overcoming the potential barrier $\Delta G(F)$ between insulating (monoclinic) and metallic (rutile) phases. Increasing pump fluence decreases the difference $N\Delta\mu$ in binding energy for these phases and, as a result, reduces the barrier. The relaxation rate for the picosecond component of SPT can be determined by the following equation [78]:

$$\tau^{-1} = \tau_0^{-1} \exp(-\Delta G(F)/k_B T), \quad (3)$$

where τ is the characteristic relaxation time and τ_0 is the shortest detectable relaxation time for this component of the SPT.

In this study, we performed a series of pump-probe measurements of VO₂ dynamics at different levels of optical excitation and then derived the time τ by an exponential fit of experimental data. We have obtained the relaxation times which compare well with the characteristic times obtained by Wall *et al.* [43] for similar processes in VO₂/SiO₂ film. The rate τ^{-1} versus pump fluence is shown in Fig. 12(b). These results can be well approximated by

$$\tau^{-1} = A F^{\tilde{N}}, \quad (4)$$

with fitting constants $A = 1.0 \times 10^{-2} \text{ cm}^2/(\text{mJ s})$ and $\tilde{N} = 1.65$. The slowest relaxation process, with the rate $\tau^{-1} = 2.9 \times 10^{10} \text{ s}^{-1}$ was still observed at pump fluence $F = 1.4 \text{ mJ/cm}^2$, which is slightly below the threshold F_0 for the femtosecond component of I-M PT discussed above. As the pump level increases to $F_{\text{max}} = 30 \text{ mJ/cm}^2$, the slower (picosecond) component of the NLO signal vanishes, providing an upper limit for the rate of SPT $\tau_0^{-1} = 2.7 \times 10^{12} \text{ s}^{-1}$.

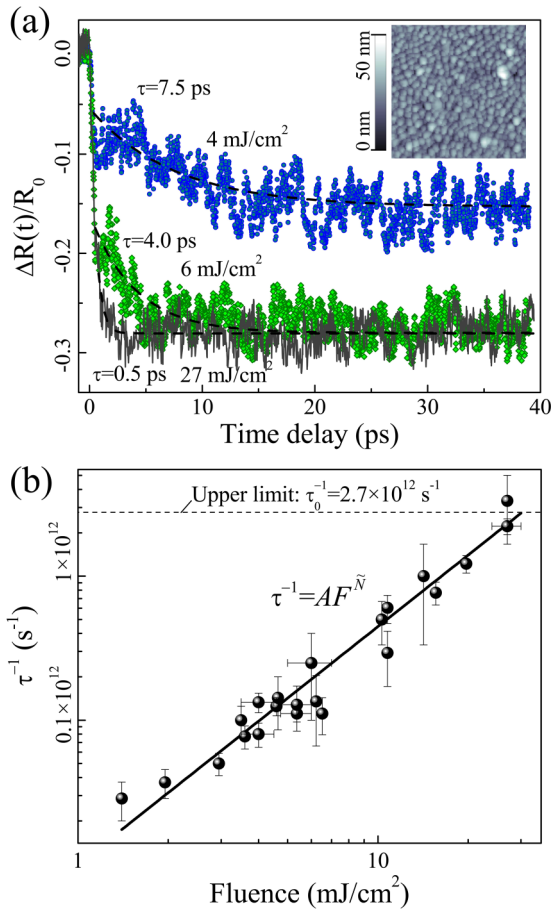


FIG. 12. (a) Transient change of $\text{VO}_2/\text{Al}_2\text{O}_3$ (C-cut) reflectivity within 40 ps at different levels of optical excitation. Dashed curves are the exponential fit. (Inset) $5 \times 5 \mu\text{m}^2$ AFM image of $\text{VO}_2/\text{Al}_2\text{O}_3$ (C-cut) sample. The average lateral size of grains is 250 nm and rms roughness is 14 nm. (b) The relaxation rate for picosecond component of photoinduced phase transition versus laser pump fluence.

Equations (3) and (4) yield the dependence of the potential barrier on pump fluence,

$$\Delta G(F) = -\tilde{N}k_B T \ln(F/F_{\text{max}}). \quad (5)$$

Figure 13(a) shows the experimentally derived ΔG versus the level of optical excitation. The fitting constant \tilde{N} in (4) and (5) can be interpreted as a constant which is proportional to the degrees of freedom and number of ions involved in the phase transition process.

Recently, the phenomenological Ginzburg-Landau formalism [89] was successfully applied to describe the second-order photoinduced phase transitions in several phase-change materials [90–93]. In our study we extend this concept to the first-order SPT in VO_2 and consider a thermodynamic potential Φ which depends on effective ion displacement η as

$$\Phi = \frac{\alpha(F)}{2}\eta^2 + \frac{\beta}{4}\eta^4 + \frac{\gamma}{6}\eta^6, \quad (6)$$

where $\alpha(F)$, β , and γ are experimentally derived constants, and $\alpha(F) > 0$, $\beta < 0$, $\gamma > 0$. In order to describe the ultrafast structural dynamics of the VO_2 lattice caused only by electronic excitations and by scattering of optical phonons within

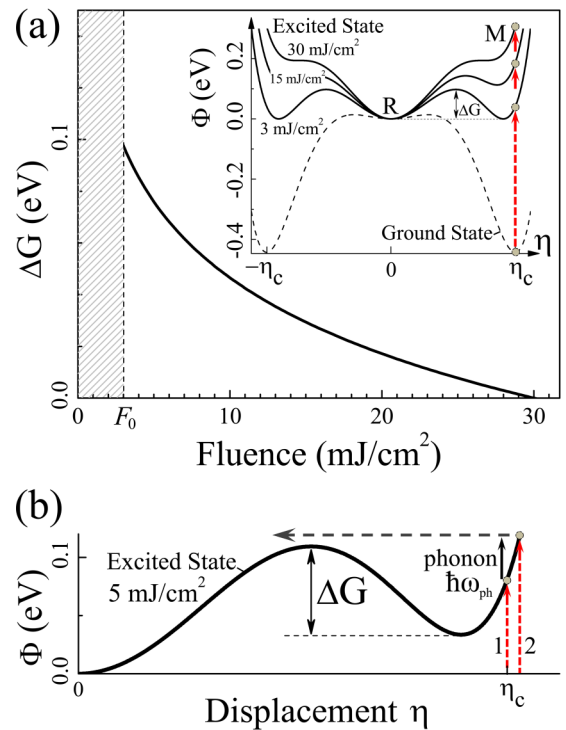


FIG. 13. (a) Potential barrier $\Delta G(F)$ between monoclinic (M) and rutile (R) phases derived from experimental data using Eq. (5). The inset shows the reconstructed thermodynamic potential Φ as a function of effective ion displacement η for the unperturbed (dashed line curve) and photoexcited (solid line curves) VO_2 . (b) The photoexcitation of VO_2 at moderate fluence. The vertical dashed arrow 1 shows the initial under-barrier energy state of the VO_2 system right after photoexcitation. In this case, the interaction of the system with an optical phonon of frequency ω_{ph} results in SPT (shown by horizontal dashed arrow). The vertical dashed arrow 2 indicates the initial over-barrier photoexcited state of VO_2 . Here the additional energy is gained by the ion subsystem via resonant excitation of Raman modes.

several picoseconds, the contribution of transient photoacoustic stress was not included in the expression (6). Using the experimentally derived potential Φ we avoid the necessity to know exact details about the nature of photoexcited states and electronic mechanism of nearly instantaneous modification of Φ by light with respect to the ground state.

Using the experimentally derived $\Delta G(F)$ [Fig. 13(a)], we performed the reconstruction of the thermodynamic potential Φ (see Supplemental Material [94]). In the unperturbed state, it has two global minima at $\pm\eta_c$ which correspond to two different domains. A VO_2 microcrystal resides only in one of these domain states. The inset in Fig. 13(a) shows the thermodynamic potential (6) as a function of effective ion displacement η for three different excitation levels. According to the Landau theory, the phase transition threshold corresponds to the case when minima of potential wells for different phases coincide.

In this study we consider the photoinduced screening of electron-electron correlations as a near-instantaneous process which occurs on a time scale comparable to or less than the duration of the femtosecond light pulse. Moreover, in

our model we assume that only this process modifies the shape of the thermodynamic potential Φ . Electron-phonon and phonon-phonon scattering processes can contribute only to the change of the energy of the ion subsystem, without altering the potential Φ . In this scenario, right after the illumination of the material by a femtosecond pulse, the electronic state of VO₂ is changed by photoexcited free carriers and is characterized by a new thermodynamic potential Φ . However, the positions of atoms remain unchanged due to the relatively slow response of the lattice to femtosecond photoexcitation. The corresponding initial states of VO₂ right after photoexcitation are marked on the Φ diagram in Figs. 13(a) and 13(b) by dashed vertical arrows. Figure 13 shows that the minimum of the potential Φ of photoexcited VO₂ no longer coincides with the minimum of the unperturbed ground state and, therefore, VO₂ is switched into a nonequilibrium state. The formation of the nonequilibrium state triggers the SPT. The quantitative modeling of subsequent structural dynamics will be given in Sec. V.

Figure 13(b) shows that at relatively low optical excitation, slightly above the threshold F_0 , the VO₂ system switches into an excited metastable state below the potential barrier $\Delta G(F)$. We note that the presence of the metastable state was directly observed previously in experiments on ultrafast electron diffraction [51,52]. In this case, the SPT occurs during several picoseconds via anharmonic scattering of optical phonons. However, a subpicosecond above-barrier pathway for the potential in Fig. 13(b) is also possible if we take into account the fact that the broadband femtosecond pulse instantaneously produces resonant Raman oscillations of the VO₂ lattice [32,33,39,49,62]. These oscillations can provide additional kinetic energy to ions, sufficient to switch the system into an excited state above the potential barrier, as indicated by the vertical dashed arrow 2 in Fig. 13(b). In this case, ion motion overcomes the barrier $\Delta G(F)$, and the structural phase transition occurs rapidly within ~ 500 fs.

If the optical pulse excites the VO₂ system below the potential barrier $\Delta G(F)$ in the Φ diagram, the SPT cannot occur due to tunneling through the barrier because of the relatively high mass of ion subsystem. However, additional energy of lattice vibrations, sufficient to overcome barrier $\Delta G(F)$, can be gained due to electron-phonon relaxation and due to anharmonic coupling of two or more optical phonons. The rate of anharmonic optical phonon scattering can be calculated using the equation obtained by Klemens [95],

$$\tau_{as}^{-1} = \omega \frac{J}{24\pi} \gamma^2 \frac{\hbar\omega}{Mv^2} \frac{a^3\omega^3}{v^3}, \quad (7)$$

where ω is the angular frequency of the phonon, M is atomic mass, a is atomic size, v is the speed of sound, γ is the Grüneisen parameter, and \hbar is Planck constant.

Parameter J ranges from 1 to 6 and corresponds to the number of different phonon scattering processes. Taking into account only single longitudinal-to-longitudinal phonon scattering, $J = 1$. The Grüneisen parameter was previously obtained only for rutile high- T metallic phase of VO₂ as $\gamma_a = \gamma_b \simeq 2.0$ and $\gamma_c \simeq 4.5$ for a_r , b_r , and c_r crystallographic directions, correspondingly [96]. In order to calculate the phonon scattering rate, we used the averaged value $\gamma = 2.8$, $\omega = 38 \times 10^{12}$ rad/s, and $v = 4000$ m/s [77]. Since the Klemens theory considers monoatomic solid such as Si, for

the case of VO₂ we used the averaged value of atomic mass $M = 4.6 \times 10^{-26}$ kg and atomic size $a = 1.9$ Å. From (7) one obtains the rate $\tau_{as}^{-1} = 1.3 \times 10^{11}$ s⁻¹. This value belongs to the range of experimentally obtained relaxation rates for the phase transition process [Fig. 12(b)] and, therefore, provides strong support for the proposed model of light-induced structural phase transition in VO₂ where anharmonic decay of optical phonons contributes to the picosecond SPT dynamics.

V. PHENOMENOLOGICAL MODEL OF ULTRAFAST STRUCTURAL DYNAMICS

The ultrafast solid-to-solid structural phase transition can be well described in terms of the phenomenological Ginzburg-Landau theory [89–93]. The oscillatory dynamics of VO₂ during the light-induced SPT is essentially nonlinear: It depends on pump fluence, film crystallinity, internal strain, and size of VO₂ grains and clusters. The metastability of phase-change material can be described by the thermodynamic potential Φ [Eq. (6)]. Previously, it was shown experimentally that the thermodynamic potential of VO₂ includes at least two lattice distortions [50,51,97,98]. However, in order to avoid possible ambiguities in the present study, we consider only a single generalized lattice distortion associated with lattice transformation from the monoclinic to rutile phase. Figure 14 shows the reconstructed potential Φ for three different levels of optical excitation. These levels correspond to the threshold laser fluence $F_0 = 3$ mJ/cm² [Fig. 14(a)], moderate excitation at $F = 10$ mJ/cm² [Fig. 14(b)], and to excitation at $F = 30$ mJ/cm² when the potential well of monoclinic phase in the Φ diagram vanishes [Fig. 14(c)].

The main pathways of lattice relaxation from monoclinic to rutile symmetry can be found by solving the motion equation for effective ion displacement η . This displacement is accompanied by photoinduced phonon oscillations with resonance frequency $\nu_0 = 6.1$ THz ($\omega = 38 \times 10^{12}$ rad/s), as shown in Fig. 9(a) and also reported in Refs. [32,33,39,43,49,62,63]. In terms of the microscopic theory of dynamic processes in structural phase transitions [99], the equation of motion can be written as

$$\tilde{m} \frac{\partial^2 \eta}{\partial t^2} + L \frac{\partial \eta}{\partial t} = -\frac{\partial \Phi}{\partial \eta}, \quad (8)$$

where \tilde{m} is effective mass of ion subsystem and L is the kinetic coefficient. According to experimental data on photoinduced coherent phonon oscillations obtained by Wall *et al.* for the subpicosecond time scale [43,63], this coefficient increases with laser fluence. Substituting (6) in (8), we find

$$\frac{\partial^2 \eta}{\omega^2 \partial t^2} + \frac{2g}{\omega^2} \frac{\partial \eta}{\partial t} + \tilde{\alpha} \eta + \tilde{\beta} \eta^3 + \tilde{\gamma} \eta^5 = 0, \quad (9)$$

where $g = L/2\tilde{m}$ corresponds to the damping of the vibrational modes, $\tilde{\alpha} = \alpha/\tilde{m}\omega^2$, $\tilde{\beta} = \beta/\tilde{m}\omega^2$, $\tilde{\gamma} = \gamma/\tilde{m}\omega^2$.

The phase trajectories on the $\eta\dot{\eta}$ phase plane and transient evolution of η in Figs. 14(d)–14(i) show possible pathways of photoinduced ultrafast lattice transformation within 1.5 ps obtained by numerical integration of Eq. (9). To perform the calculations, the kinetic coefficients were estimated from previously obtained experimental data of photoinduced phase transition, yielding $g = 3.3 \times 10^{12}$ s⁻¹ ($F_0 = 3$ mJ/cm²),

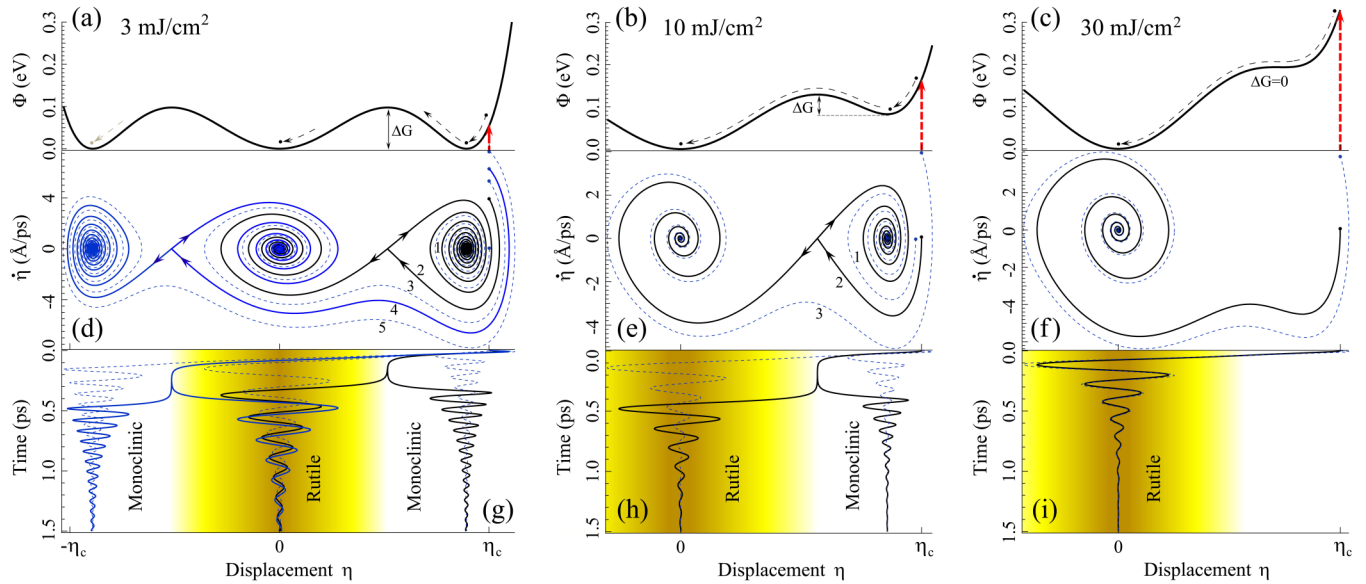


FIG. 14. Thermodynamic potential Φ , phase trajectories on the $\eta\dot{\eta}$ phase plane, and evolution of $\eta(t)$ at different levels of optical excitation: at threshold laser fluence $F_0 = 3 \text{ mJ/cm}^2$ (a), (d), (g); at $F = 10 \text{ mJ/cm}^2$ (b), (e), (h); and at $F = 30 \text{ mJ/cm}^2$ (c), (f), (i). Vertical dashed arrows on Φ diagrams show the initial energy of the VO_2 system right after photoexcitation at $\eta(0) = \eta_c$.

$g = 5.0 \times 10^{12} \text{ s}^{-1}$ ($F = 10 \text{ mJ/cm}^2$), and $g = 5.2 \times 10^{12} \text{ s}^{-1}$ ($F = 30 \text{ mJ/cm}^2$). We note that these damping constants are sufficiently close to the constants which can be derived from damping ratio obtained in Ref. [43]. The effective mass \tilde{m} was estimated at the threshold fluence F_0 as $\tilde{m} = 1.7 \times 10^{-25} \text{ kg}$ using experimentally obtained constants for the potential $\Phi(F_0)$ (see Supplemental Material [94]).

As shown above, the characteristic time of SPT and, as a result, the kinetic coefficient depends on grain size. A presence of structural defects, local deformations, and inhomogeneous strains between domain boundaries or neighboring grains alters the profile of thermodynamic potential Φ [Fig. 9(b)]. These factors, and also the resonant excitation of coherent optical phonons, can contribute into different pathways of the SPT dynamics upon optical excitation, as shown in Figs. 14(d)–14(i).

As was experimentally observed in this work, the optical signal related to the fastest component of the phase transition (i.e., rapid change of the optical signal within $\sim 500 \text{ fs}$) at threshold excitation level $F_0 = 3 \text{ mJ/cm}^2$ is relatively small. However, as excitation increases, the amplitude of this signal asymptotically increases and approaches some constant level [see Figs. 5 and 12(a)]. Above $F \sim 10\text{--}15 \text{ mJ/cm}^2$ the signal nearly saturates, but still follows by a minor component of slower (picosecond) evolution. The picosecond component of the NLO signal vanishes above $F = 30 \text{ mJ/cm}^2$ [see Fig. 12(b)]. The modeling of ultrafast structural dynamics in Fig. 14 fully supports the experimentally observed NLO dynamics of VO_2 .

According to the model, at threshold fluence $F_0 = 3 \text{ mJ/cm}^2$ the optical pulse excites the system below the potential barrier ΔG which separates two phases [Fig. 14(a)]. Such excitation returns the system back to its monoclinic phase: The system does not overcome the ΔG barrier and relaxes to the bottom of the potential well which corresponds to the excited (and also slightly *distorted*) metastable monoclinic phase. The

corresponding trajectory in the $\eta\dot{\eta}$ diagram [Fig. 14(d)] is a spiral dashed curve 1. The frequency of dissipative oscillations during this relaxation is nearly double the frequency ν_0 and is $\sim 12 \text{ THz}$ [Fig. 14(g)]. It is important to note that very similar oscillatory dynamics with 11.2-THz frequency was experimentally observed in this study (Fig. 10). Also, 12-THz and 10-THz oscillations were observed, respectively, by Pashkin *et al.* [33] and by Wall *et al.* [43] in the low-fluence regime. These facts strongly support the correctness of the model proposed.

Different trajectories of SPT in Fig. 14 are defined by different initial conditions during photoexcitation of the material. An additional contribution to the ultrafast SPT can be produced by the resonant Raman process. Coherent Raman excitation of the lattice is a nearly instantaneous process which occurs within the time scale of light interaction with the sample. This process can provide additional kinetic energy to the system, switching it to the phase trajectories 2–5 in Figs. 14(d) and 14(g). Trajectory 2 is a separatrix which corresponds to the case when the system passes a saddle point and can be switched either to the rutile or monoclinic phase. Trajectory 3 is the transition to the metallic rutile phase.

It is interesting to note the possibility of switching VO_2 into another domain state of the monoclinic phase. Separatrix 4 and trajectory 5 in Figs. 14(d) and 14(g) show the relaxation of VO_2 into the second potential well of the monoclinic phase, related to another domain state. Here we only mention this possibility which could be potentially observed [100]. However, this requires verification by additional rigorous experimental studies of photoinduced dynamics.

According to the model of SPT shown in Fig. 13, the photoinduced screening of electron correlations is a nearly instantaneous process which alters only the thermodynamic potential. If the coherent Raman process is excluded from the consideration, the photoinduced screening does not change directly the position of ions, and does not provide additional

kinetic energy and momentum to the ion subsystem. In this case the most probable trajectory will correspond to the trajectory with initial parameters $\eta(0) = \eta_c$ and $\dot{\eta}(0) = 0$. Figure 14(e) shows that this is a separatrix (trajectory 2) for moderate excitation $F = 10 \text{ mJ/cm}^2$. That is, above $F = 10 \text{ mJ/cm}^2$ the majority of phase trajectories lead to complete structural transition. This dynamics corresponds to subpicosecond SPT of mostly all volume of the material. This is supported by our experimental observations of the fastest (subpicosecond) component of SPT dynamics. It was found that the transient reflectance within $\sim 1 \text{ ps}$ time scale nearly saturates as pump fluence approaches $F \sim 10\text{--}15 \text{ mJ/cm}^2$ [see Figs. 5 and 12(a)]. Rigorous measurements of transient reflectivity versus excitation fluence performed by Wall *et al.* in Ref. [63] shows very similar saturation of the transient reflectivity signal as the fluence approaches $F \sim 20 \text{ mJ/cm}^2$. We also note that there is still some possibility of relaxation back to monoclinic phase (trajectory 1) [Figs. 14(e) and 14(h)]. In this case, the SPT occurs via optical phonon scattering during several picoseconds, as discussed above. This slower relaxation is observed up to $F = 30 \text{ mJ/cm}^2$ [Fig. 12(b)].

At an excitation level of $F = 30 \text{ mJ/cm}^2$ the system dynamics undergoes a qualitative change: The potential well of monoclinic phase and barrier ΔG vanishes [Fig. 14(c)]. As a result, all possible phase trajectories change the symmetry of VO₂ from monoclinic to rutile [Figs. 14(f) and 14(i)]. No slow (picosecond) relaxation component was observed in the NLO signal above $F = 30 \text{ mJ/cm}^2$, since there is no pathway to the metastable monoclinic phase.

The proposed model describes the ultrafast structural dynamics within several picoseconds after photoexcitation and agrees with numerous experimental observations of the SPT in VO₂. In order to extend this model on the nanosecond time scale, the model has to include additional modulation of thermodynamic potential by acoustic strain as well as a growth of phonon entropy [101].

VI. CONCLUSION

It was demonstrated that the photoexcitation of VO₂ enables various pathways and possibilities for transformation from its monoclinic to rutile symmetry. Resulting dynamics strongly depends on the excitation level, film morphology, internal strain, and strain induced by the optical pulse.

Semiclassical computation of molecular dynamics for VO₂ reveals significant instability of the monoclinic phase in the absence of electron-electron correlations. The computed dynamics of the VO₂ lattice shows its close resemblance to the experimentally observed transient NLO response of VO₂ on the subpicosecond time scale. The thermodynamic parameters obtained by the MD method show that the screening of electron

correlations results in an exothermic reaction with saturation of the phonon spectrum at initial temperatures of VO₂ as low as $T = 15 \text{ K}$. Also, calculations show the relatively small influence of structural point defects on kinetics of SPT. This was supported by experimental study of photoinduced dynamics of nonepitaxial films with a relatively high concentration of defects. Nevertheless, a presence of structural defects produces nonuniform metallic phase nucleation on the subpicosecond time scale.

On a few-picosecond time scale the structural phase transition can be considered as a nonthermal process. However, on the nanosecond time scale the thermal contribution to the transition becomes essential. It was also shown that photoacoustic stress can potentially induce a ferroelastic phase transition. Thus, the pronounced oscillatory signal which could be associated with alternating switching of the VO₂ phase by a photoacoustic wave was observed at frequency 0.8 GHz [Fig. 6(e)].

It was shown that the internal misfit strain in epitaxial film noticeably alters the rate of phase transition within $\sim 500 \text{ fs}$. For epitaxial films with anisotropic strain the phase transition rate depends on the size and in-plane orientation of VO₂ grains/domains. This evidences that the strain alters the potential energy landscape of photoexcited VO₂ and, as a result, changes the phase trajectory of ultrafast structural dynamics.

In this work, we proposed a technique for a quantitative reconstruction of the thermodynamic potential of photoexcited phase-change material. While it is rather an estimation of the energy landscape versus pump fluence, the obtained energy can be used for semiquantitative analysis and numerical modeling of photoinduced dynamics. We show that the modeling of ultrafast processes in VO₂ can be performed in terms of a phenomenological Ginzburg-Landau model. This model provides a reliable explanation of experimentally observed structural dynamics, where the phase trajectories depend on the excitation level. Thus, higher optical excitation above $\sim 30 \text{ mJ/cm}^2$ corresponds to complete structural transition of all VO₂ grains/domains into the metallic rutile phase within $\sim 500 \text{ fs}$. However, at lower excitations, grains/domains can be turned to long-lived the metastable monoclinic phase. The presented approach to model the photoinduced structural dynamics offers unique potential for the study of different phase-change materials.

ACKNOWLEDGMENTS

We wish to thank Dr. Andrey Akimov for valuable discussions and comments. The authors gratefully acknowledge support from the U.S. Army Research Laboratory and the U.S. Army Research Office under Contract No. W911NF-15-1-0448.

[1] F. J. Morin, *Phys. Rev. Lett.* **3**, 34 (1959).

[2] K. Okimura, J. Sakai, and S. Ramanathan, *J. Appl. Phys.* **107**, 063503 (2010).

[3] J. D. Budai, A. Tselev, J. Z. Tischler, E. Strelcov, A. Kolmakov, W. J. Liu, A. Gupta, and J. Narayan, *Acta Mater.* **61**, 2751 (2013).

- [4] G. Andersson, *Acta Chem. Scand.* **10**, 623 (1956).
- [5] J. M. Longo and P. Kierkegaard, *Acta Chem. Scand.* **24**, 420 (1970).
- [6] S. Westman, *Acta Chem. Scand.* **15**, 217 (1961).
- [7] M. Liu, A. J. Sternbach, M. Wagner, T. V. Slusar, T. Kong, S. L. Bud'ko, S. Kittiwatanakul, M. Qazilbash, A. McLeod, Z. Fei *et al.*, *Phys. Rev. B* **91**, 245155 (2015).
- [8] J. H. Park, J. M. Coy, T. S. Kasirga, C. Huang, Z. Fei, S. Hunter, and D. H. Cobden, *Nature (London)* **500**, 431 (2013).
- [9] J. Pouget, H. Launois, T. Rice, P. Dernier, A. Gossard, G. Villeneuve, and P. Hagenmuller, *Phys. Rev. B* **10**, 1801 (1974).
- [10] A. Zylbersztejn and N. F. Mott, *Phys. Rev. B* **11**, 4383 (1975).
- [11] H. Nakatsugawa and E. Iguchi, *Phys. Rev. B* **55**, 2157 (1997).
- [12] M. S. Laad, L. Craco, and E. Müller-Hartmann, *Phys. Rev. B* **73**, 195120 (2006).
- [13] V. Eyert, *Ann. Phys. (Leipzig)* **11**, 650 (2002).
- [14] V. Eyert, *Phys. Rev. Lett.* **107**, 016401 (2011).
- [15] J. B. Goodenough, *J. Solid State Chem.* **3**, 490 (1971).
- [16] D. Paquet and P. Leroux-Hugon, *Phys. Rev. B* **22**, 5284 (1980).
- [17] T. Koethe, Z. Hu, M. Haverkort, C. Schüßler-Langeheine, F. Venturini, N. Brookes, O. Tjernberg, W. Reichelt, H. Hsieh, H.-J. Lin *et al.*, *Phys. Rev. Lett.* **97**, 116402 (2006).
- [18] M. Gatti, F. Bruneval, V. Olevano, and L. Reining, *Phys. Rev. Lett.* **99**, 266402 (2007).
- [19] J. Cao, E. Ertekin, V. Srinivasan, W. Fan, S. Huang, H. Zheng, J. W. L. Yim, D. R. Khanal, D. F. Ogletree, J. C. Grossman *et al.*, *Nat. Nanotechnol.* **4**, 732 (2009).
- [20] A. Tselev, V. Meunier, E. Strelcov, W. A. Shelton, I. A. Luk'yanchuk, K. Jones, R. Proksch, A. Kolmakov, and S. V. Kalinin, *ACS Nano* **4**, 4412 (2010).
- [21] J. P. Pouget, H. Launois, J. d'Haenens, P. Merenda, and T. M. Rice, *Phys. Rev. Lett.* **35**, 873 (1975).
- [22] M. Liu, M. Wagner, J. Zhang, A. McLeod, S. Kittiwatanakul, Z. Fei, E. Abreu, M. Goldflam, A. J. Sternbach, S. Dai *et al.*, *Appl. Phys. Lett.* **104**, 121905 (2014).
- [23] A. Pergament, P. Boriskov, A. Velichko, and N. Kuldin, *J. Phys. Chem. Solids* **71**, 874 (2010).
- [24] H.-T. Kim, B.-J. Kim, Y. W. Lee, B.-G. Chae, and S. J. Yun, *Phys. B* **403**, 1434 (2008).
- [25] A. Crunteanu, J. Givernaud, J. Leroy, D. Mardivirin, C. Champeaux, J.-C. Orlianges, A. Catherinot, and P. Blondy, *Sci. Tech. Adv. Mater.* **11**, 065002 (2010).
- [26] Y. Jiazhen, Z. Yue, H. Wanxia, and T. Mingjin, *Thin Solid Films* **516**, 8554 (2008).
- [27] W. Burkhardt, T. Christmann, S. Franke, W. Kriegseis, D. Meister, B. Meyer, W. Niessner, D. Schalch, and A. Scharmann, *Thin Solid Films* **402**, 226 (2002).
- [28] B. Mayer, C. Schmidt, A. Grupp, J. Bühler, J. Oelmann, R. E. Marvel, R. Haglund Jr, T. Oka, D. Brida, A. Leitenstorfer *et al.*, *Phys. Rev. B* **91**, 235113 (2015).
- [29] K. Appavoo, D. Y. Lei, Y. Sonnefraud, B. Wang, S. T. Pantelides, S. A. Maier, and R. F. Haglund, *Nano Lett.* **12**, 780 (2012).
- [30] W. Roach and I. Balberg, *Solid State Commun.* **9**, 551 (1971).
- [31] T. L. Cocker, L. V. Titova, S. Fourmaux, G. Holloway, H.-C. Bandulet, D. Brassard, J.-C. Kieffer, M. A. El Khakani, and F. A. Hegmann, *Phys. Rev. B* **85**, 155120 (2012).
- [32] C. Kübler, H. Ehrke, R. Huber, R. Lopez, A. Halabica, R. F. Haglund, and A. Leitenstorfer, *Phys. Rev. Lett.* **99**, 116401 (2007).
- [33] A. Pashkin, C. Kübler, H. Ehrke, R. Lopez, A. Halabica, R. F. Haglund, R. Huber, and A. Leitenstorfer, *Phys. Rev. B* **83**, 195120 (2011).
- [34] D. Wegkamp and J. Stähler, *Progr. Surf. Sci.* **90**, 464 (2015).
- [35] Z. He and A. J. Millis, *Phys. Rev. B* **93**, 115126 (2016).
- [36] V. Vikhnin, S. Lysenko, A. Rua, F. Fernandez, and H. Liu, *Solid State Commun.* **137**, 615 (2006).
- [37] M. van Veenendaal, *Phys. Rev. B* **87**, 235118 (2013).
- [38] D.-S. Yang, P. Baum, and A. H. Zewail, *Struct. Dyn.* **3**, 034304 (2016).
- [39] A. Cavalleri, T. Dekorsy, H. H. W. Chong, J. C. Kieffer, and R. W. Schoenlein, *Phys. Rev. B* **70**, 161102 (2004).
- [40] M. Hada, D. Zhang, A. Casandru, R. J. Dwayne Miller, Y. Hontani, J. Matsuo, R. E. Marvel, and R. F. Haglund, Jr., *Phys. Rev. B* **86**, 134101 (2012).
- [41] H. Wen, L. Guo, E. Barnes, J. H. Lee, D. A. Walko, R. D. Schaller, J. A. Moyer, R. Misra, Y. Li, E. M. Dufresne *et al.*, *Phys. Rev. B* **88**, 165424 (2013).
- [42] S. Lysenko, V. Vikhnin, F. Fernandez, A. Rua, and H. Liu, *Phys. Rev. B* **75**, 075109 (2007).
- [43] S. Wall, L. Foglia, D. Wegkamp, K. Appavoo, J. Nag, R. F. Haglund, J. Stähler, and M. Wolf, *Phys. Rev. B* **87**, 115126 (2013).
- [44] C. Chen, Y. Zhao, X. Pan, V. Kuryatkov, A. Bernussi, M. Holtz, and Z. Fan, *J. Appl. Phys.* **110**, 023707 (2011).
- [45] M. A. Huber, M. Plankl, M. Eisele, R. E. Marvel, F. Sandner, T. Korn, C. Schüller, R. Haglund Jr., R. Huber, and T. L. Cocker, *Nano Lett.* **16**, 1421 (2016).
- [46] D. Wegkamp, M. Herzog, L. Xian, M. Gatti, P. Cudazzo, C. L. McGahan, R. E. Marvel, R. F. Haglund Jr., A. Rubio, M. Wolf *et al.*, *Phys. Rev. Lett.* **113**, 216401 (2014).
- [47] C. Ott, M. F. Jager, C. J. Kaplan, R. E. Marvel, R. F. Haglund, D. M. Neumark, and S. R. Leone, *International Conference on Ultrafast Phenomena, Santa Fe, New Mexico United States* (Optical Society of America, Washington, D.C., 2016), p. UM1A-3.
- [48] N. F. Mott, *Rev. Mod. Phys.* **40**, 677 (1968).
- [49] B. T. O'Callahan, A. C. Jones, J. H. Park, D. H. Cobden, J. M. Atkin, and M. B. Raschke, *Nat. Commun.* **6**, 6849 (2015).
- [50] P. Baum, D.-S. Yang, and A. H. Zewail, *Science* **318**, 788 (2007).
- [51] Z. Tao, F. Zhou, T.-R. T. Han, D. Torres, T. Wang, N. Sepulveda, K. Chang, M. Young, R. R. Lunt, and C.-Y. Ruan, *Sci. Rep.* **6**, 38514 (2016).
- [52] V. R. Morrison, R. P. Chatelain, K. L. Tiwari, A. Hendaoui, A. Bruhács, M. Chaker, and B. J. Siwick, *Science* **346**, 445 (2014).
- [53] Computer code QUANTUMWISE A/S, Atomistix ToolKit, Copenhagen, 2014.
- [54] A. C. T. van Duin, S. Dasgupta, F. Lorant, and W. A. Goddard III, *J. Phys. Chem. A* **105**, 9396 (2001).
- [55] K. Chenoweth, A. C. Van Duin, and W. A. Goddard III, *J. Phys. Chem. A* **112**, 1040 (2008).
- [56] M. Griebel, S. Knapek, and G. Zumbusch, *Numerical Simulation in Molecular Dynamics: Numerics, Algorithms, Parallelization, Applications* (Springer-Verlag, Berlin/Heidelberg, 2007).
- [57] S. Lysenko, V. Vikhnin, A. Rúa, F. Fernández, and H. Liu, *Phys. Rev. B* **82**, 205425 (2010).

- [58] H. J. G. J. Ryder, F. S. L. Hsu, and J. E. Kunzler, *Phys. Rev.* **185**, 1022 (1969).
- [59] G. V. Chandrashekar, H. Barros, and J. Honig, *Mater. Res. Bull.* **8**, 369 (1973).
- [60] J. M. Ziman, *Electrons and Phonons: The Theory of Transport Phenomena in Solids* (Oxford University Press, New York, 1960).
- [61] S.-T. Lin, M. Blanco, and W. A. Goddard III, *J. Chem. Phys.* **119**, 11792 (2003).
- [62] H.-T. Kim, Y. W. Lee, B.-J. Kim, B.-G. Chae, S. J. Yun, K.-Y. Kang, K.-J. Han, K.-J. Yee, and Y.-S. Lim, *Phys. Rev. Lett.* **97**, 266401 (2006).
- [63] S. Wall, D. Wegkamp, L. Foglia, K. Appavoo, J. Nag, R. Haglund Jr., J. Stähler, and M. Wolf, *Nat. Commun.* **3**, 721 (2012).
- [64] M. Borek, F. Qian, V. Nagabushnam, and R. K. Singh, *Appl. Phys. Lett.* **63**, 3288 (1993).
- [65] F. C. Case, *J. Vac. Sci. Technol. A* **2**, 1509 (1984).
- [66] J. F. De Natale, P. J. Hood, and A. B. Harker, *J. Appl. Phys.* **66**, 5844 (1989).
- [67] Z. P. Wu, A. Miyashita, I. Nashiyama, and H. Naramoto, *Philos. Mag. Lett.* **79**, 813 (1999).
- [68] S. Lysenko, A. Rúa, V. Vikhnin, F. Fernández, and H. Liu, *Phys. Rev. B* **76**, 035104 (2007).
- [69] S. Lysenko, A. Rúa, F. Fernandez, and H. Liu, *J. Appl. Phys.* **105**, 043502 (2009).
- [70] V. Sterligov and P. Cheyssac, French Patent No. 0115232 (2001).
- [71] J. C. Stover, *Optical Scattering: Measurement and Analysis* (SPIE Optical Engineering Press, Bellingham, 1995).
- [72] N. F. Brady, K. Appavoo, M. Seo, J. Nag, R. P. Prasankumar, R. F. Haglund Jr., and D. J. Hilton, *J. Phys. Condens. Matter* **28**, 125603 (2016).
- [73] D. J. Hilton, R. P. Prasankumar, S. Fourmaux, A. Cavalleri, D. Brassard, M. A. El Khakani, J. C. Kieffer, A. J. Taylor, and R. D. Averitt, *Phys. Rev. Lett.* **99**, 226401 (2007).
- [74] A. C. Diebold, *Handbook of Silicon Semiconductor Metrology* (CRC Press, New York/Basel, 2001).
- [75] C. Thomsen, J. Strait, Z. Vardeny, H. J. Maris, J. Tauc, and J. J. Hauser, *Phys. Rev. Lett.* **53**, 989 (1984).
- [76] C. Thomsen, H. T. Grahm, H. J. Maris, and J. Tauc, *Phys. Rev. B* **34**, 4129 (1986).
- [77] D. Maurer, A. Leue, R. Heichele, and V. Müller, *Phys. Rev. B* **60**, 13249 (1999).
- [78] K. H. Bennemann, *J. Phys. Condens. Matter* **23**, 073202 (2011).
- [79] E. Abreu, S. N. G. Corder, S. J. Yun, S. Wang, J. G. Ramirez, K. West, J. Zhang, S. Kittiwatanakul, I. K. Schuller, J. Lu, S. A. Wolf, H.-T. Kim, M. Liu, and R. D. Averitt, [arXiv:1701.05531](https://arxiv.org/abs/1701.05531).
- [80] S. Lysenko, F. Fernández, A. Rúa, N. Sepúlveda, and J. Aparicio, *Appl. Opt.* **54**, 2141 (2015).
- [81] S. Lysenko, A. Rúa, and F. Fernández, *International Conference on Ultrafast Phenomena, Santa Fe, New Mexico United States* (Optical Society of America, Washington, D.C., 2016), p. UTu4A.48.
- [82] E. R. Dobrovinskaya, L. A. Lytvynov, and V. Pishchik, *Sapphire: Material, Manufacturing, Applications* (Springer Science & Business Media, New York, 2009).
- [83] H. W. Verleur, A. S. Barker, and C. N. Berglund, *Phys. Rev.* **172**, 788 (1968).
- [84] S. Lysenko, F. Fernandez, A. Rúa, and H. Liu, *J. Appl. Phys.* **114**, 153514 (2013).
- [85] J. M. Elson, *Waves Random Media* **7**, 303 (1997).
- [86] J. Y. Suh, R. Lopez, L. C. Feldman, and R. F. Haglund, *J. Appl. Phys.* **96**, 1209 (2004).
- [87] H. Katzke, P. Toledano, and W. Depmeier, *Phys. Rev. B* **68**, 024109 (2003).
- [88] K. Appavoo, B. Wang, N. F. Brady, M. Seo, J. Nag, R. P. Prasankumar, D. J. Hilton, S. T. Pantelides, and R. F. Haglund, *Nano Lett.* **14**, 1127 (2014).
- [89] Landau and Lifshitz, *Statistical Physics, Part 1* (Elsevier, Butterworth Heinemann, 1980).
- [90] C. Giannetti, M. Capone, D. Fausti, M. Fabrizio, F. Parmigiani, and D. Mihailovic, *Adv. Phys.* **65**, 58 (2016).
- [91] R. Yusupov, T. Mertelj, V. V. Kabanov, S. Brazovskii, P. Kusar, J.-H. Chu, I. R. Fisher, and D. Mihailovic, *Nat. Phys.* **6**, 681 (2010).
- [92] T. Huber, S. O. Mariager, A. Ferrer, H. Schäfer, J. A. Johnson, S. Grübel, A. Lübcke, L. Huber, T. Kubacka, C. Dornes *et al.*, *Phys. Rev. Lett.* **113**, 026401 (2014).
- [93] P. Beaud, A. Caviezel, S. Mariager, L. Rettig, G. Ingold, C. Dornes, S. Huang, J. Johnson, M. Radovic, T. Huber *et al.*, *Nat. Mater.* **13**, 923 (2014).
- [94] See Supplemental Material at <http://link.aps.org/supplemental/10.1103/PhysRevB.96.075128> for reconstruction of the thermodynamic potential of photoexcited VO₂.
- [95] P. G. Klemens, *Phys. Rev.* **148**, 845 (1966).
- [96] C. Hearn, *Solid State Commun.* **13**, 1139 (1973).
- [97] A. X. Gray, M. C. Hoffmann, J. Jeong, N. P. Aetukuri, D. Zhu, H. Y. Hwang, N. C. Brandt, H. Wen, A. J. Sternbach, S. Bonetti *et al.*, [arXiv:1601.7490](https://arxiv.org/abs/1601.7490).
- [98] N. Kumar, A. Rúa, F. E. Fernandez, and S. Lysenko, *Phys. Rev. B* **95**, 235157 (2017).
- [99] B. A. Strukov and A. P. Levanyuk, *Ferroelectric Phenomena in Crystals: Physical Foundations* (Springer, Berlin/Heidelberg, 1998).
- [100] S. A. Dönges, O. Khatib, B. T. O'Callahan, J. M. Atkin, J. H. Park, D. Cobden, and M. B. Raschke, *Nano Lett.* **16**, 3029 (2016).
- [101] J. D. Budai, J. Hong, M. E. Manley, E. D. Specht, C. W. Li, J. Z. Tischler, D. L. Abernathy, A. H. Said, B. M. Leu, L. A. Boatner, R. J. McQueeney, and O. Delaire, *Nature (London)* **515**, 535 (2014).

Supplementary Information

Ultrafast Structural Dynamics of VO₂

Sergiy Lysenko, Nardeep Kumar, Armando Rúa, José Figueroa, Junqiang Lu, and Félix Fernández
Department of Physics, University of Puerto Rico, Mayaguez, Puerto Rico 00681, USA

RECONSTRUCTION OF THE THERMODYNAMIC POTENTIAL

We discuss the reconstruction of the thermodynamic potential Φ for the case of photoinduced first-order phase transition. The potential Φ is considered as the Landau expansion of the free energy [1] for the effective displacement of lattice ions η in the following form

$$\Phi = \frac{\alpha}{2}\eta^2 + \frac{\beta}{4}\eta^4 + \frac{\gamma}{6}\eta^6, \quad (1)$$

where α , β , and γ are constants, and $\alpha > 0$, $\beta < 0$, $\gamma > 0$, and $\alpha \equiv \alpha(F)$. The constant α can be considered as the quasiharmonic constant. β and γ are fourth- and sixth-order generalized constants. In Eq.(1) we assume that α is the only constant which depends on the excitation fluence F . In this study we will find the constants $\alpha(F)$, β and γ .

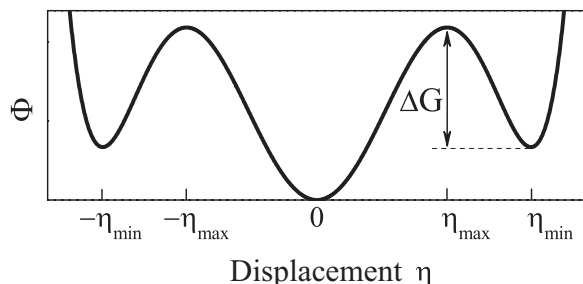


FIG. 1: Thermodynamic potential of the material in nonequilibrium state.

Figure. 1 shows a typical profile of the potential Φ described by the Eq.(1). The condition $\partial\Phi/\partial\eta=0$ yields the positions of minima η_{min} and maxima η_{max}

$$\eta_{min,max} = \sqrt{\frac{-\beta \pm \sqrt{\beta^2 - 4\alpha\gamma}}{2\gamma}}. \quad (2)$$

η_{min} and η_{max} can be used to calculate the energy barrier ΔG which separates two structural phases of VO₂

$$\Delta G = \Phi(\eta_{max}) - \Phi(\eta_{min}). \quad (3)$$

Figure 2 shows the potential Φ at the threshold fluence F_0 for the structural phase transition of VO₂. For this

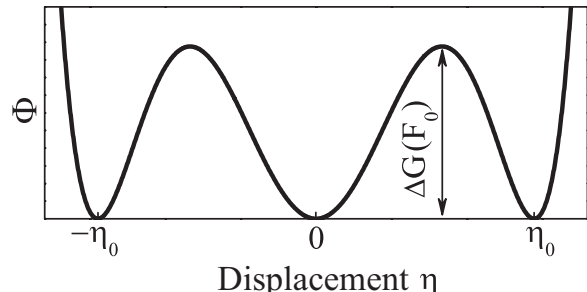


FIG. 2: Thermodynamic potential at the threshold excitation fluence F_0 .

state one can obtain the following coupled equations

$$\left. \begin{aligned} \frac{\partial\Phi(\eta_0, F_0)}{\partial\eta} &= \alpha_0\eta_0 + \beta\eta_0^3 + \gamma\eta_0^5 = 0 \\ \Phi(\eta_0, F_0) &= \frac{\alpha_0}{2}\eta_0^2 + \frac{\beta}{4}\eta_0^4 + \frac{\gamma}{6}\eta_0^6 = 0 \end{aligned} \right\} \quad (4)$$

where the constants $\alpha_0 = \alpha(F_0)$ and $\eta_0 = \eta_{min}$ at F_0 . The solution of (4) yields the relations between constants

$$\beta = -\frac{4\alpha_0}{\eta_0^2}, \quad (5)$$

$$\gamma = \frac{3\alpha_0}{\eta_0^4}, \quad (6)$$

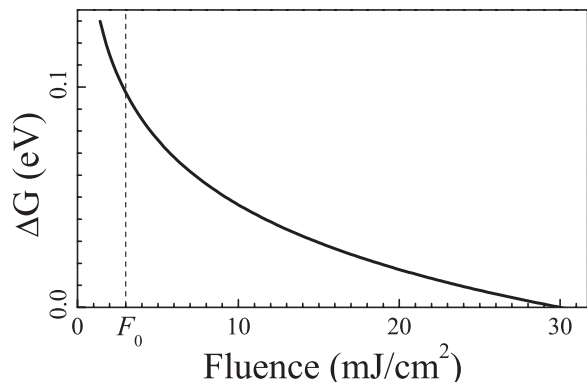


FIG. 3: Potential barrier $\Delta G(F)$ between two structural phases of VO₂ derived from experimental data, as described in the main text of the paper.

The reconstruction of the potential Φ can be stated with arbitrary units for the effective displacement η , setting $\eta_0 = 1$. Using the experimentally obtained function

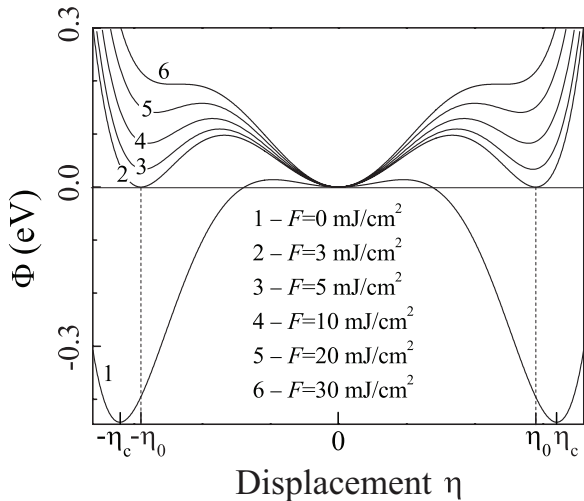


FIG. 4: Thermodynamic potential as a function of effective ion displacement η for different levels of optical excitation.

$\Delta G(F)$ (Fig. 3), Eq.(3) and the condition $\Delta G(\alpha_0) = \Delta G(F_0)$, we obtain numerically the constant α_0 at the threshold level F_0

$$\left. \begin{aligned} \Delta G(\alpha_0) &= \Phi(\eta_{max}[\alpha_0]) - \Phi(\eta_{min}[\alpha_0]) \\ \Delta G(\alpha_0) &= \Delta G(F_0) \end{aligned} \right\} \implies \alpha_0 \implies \beta, \gamma. \quad (7)$$

The constants β and γ are calculated according to (5) and (6). These constants do not depend on excitation fluence F . The profile of the potential Φ at different levels of photoexcitation is altered only by the constant $\alpha(F)$. In order to find the dependence of α versus F , the potential barrier was calculated numerically as a function of α . Then, these data were presented as $\alpha(\Delta G)$

$$\Delta G(\alpha) = \Phi(\eta_{max}[\alpha]) - \Phi(\eta_{min}[\alpha]) \implies \alpha(\Delta G) \quad (8)$$

The function $\Delta G(F)$ (Fig. 3) was obtained experimentally, as described in the main text of the paper. These data yield the dependence of the fluence versus the value of potential barrier, $F(\Delta G)$. Thus, by calculating the $\alpha(\Delta G)$ and $F(\Delta G)$ at the same values of ΔG one can obtain numerically the function $\alpha(F)$.

$$\left. \begin{aligned} \alpha(\Delta G) \\ F(\Delta G) \end{aligned} \right\} \implies \alpha(F) \quad (9)$$

As the function $\alpha(F)$ is obtained, the potential $\Phi(F)$ can be calculated at different pump fluences using the expression (1), as shown in Fig. 4. For the ground state, the constant $\alpha(0)$ was estimated by extrapolation of the experimental data. We note that while the absolute values of constants α , β , and γ depend on the dimension of the displacement η , the reconstructed energy profile does

not. If the value of the effective displacement of lattice ions η_c for the ground state is known, then all constants can be easily renormalized.

The computation of molecular dynamics (MD) shows that the root-mean-square (*rms*) displacement of VO₂ atoms within the first 500 fs after photoexcitation is 0.32 Å. Using this value as η_c , one obtains $\eta_0 = 0.29$ Å. While the rms displacement is not, strictly speaking, an order parameter of photoinduced structural phase transition, it compares well with the effective displacement of VO₂ ions (0.26 Å) obtained recently by van Veenendaal [2]. Taking into account a proximity between these values within ~ 500 fs, the value obtained by MD computation was considered as a reasonable estimation of the effective ions displacement η_c for our study.

Table I shows constants $\alpha(F)$, β and γ , and energy barriers ΔG obtained for different levels of optical excitation. These constants were used for the modeling of the phase trajectories (Sec.V in the main text of the paper). For the photoexcited VO₂, the most pronounced ~ 6 THz oscillations of the optical signal have been observed at the threshold excitation in several experimental works [3–7]. In our study we obtained the frequency of 6.1 THz ($\omega = 38.3 \times 10^{12}$ rad/s). Assuming that at the threshold level the quasiharmonic constant is $\alpha_0 \simeq \tilde{m}\omega^2$, and also $\alpha_0 = 251.92034$ J/m² (see Table I for $F_0 = 3$ mJ/cm²), one obtains the effective mass $\tilde{m} = 1.71 \times 10^{-25}$ kg. We note that this value is 2.4 times lower than the effective mass $\tilde{m} = 4.06 \times 10^{-25}$ kg of the ions involved in structural distortion, as used by van Veenendaal in his theoretical work to describe the light-induced phase transition in VO₂ [2]. The discrepancy in the effective masses of the ion subsystem is related to the difference in the models and approaches applied to describe the nonequilibrium structural dynamics of VO₂.

-
- [1] Landau and Lifshitz, *Statistical Physics, Part 1* (Elsevier, Butterworth Heinemann, 1980).
 - [2] M. van Veenendaal, Phys. Rev. B **87**, 235118 (2013).
 - [3] A. Cavalleri, T. Dekorsy, H. H. W. Chong, J. C. Kieffer, and R. W. Schoenlein, Phys. Rev. B **70**, 161102 (2004).
 - [4] H.-T. Kim, Y. W. Lee, B.-J. Kim, B.-G. Chae, S. J. Yun, K.-Y. Kang, K.-J. Han, K.-J. Yee, and Y.-S. Lim, Phys. Rev. Lett. **97**, 266401 (2006).
 - [5] C. Kübler, H. Ehrke, R. Huber, R. Lopez, A. Halabica, R. F. Haglund, and A. Leitnerstorfer, Phys. Rev. Lett. **99**, 116401 (2007).
 - [6] S. Wall, L. Foglia, D. Wegkamp, K. Appavoo, J. Nag, R. F. Haglund, J. Stähler, and M. Wolf, Phys. Rev. B **87**, 115126 (2013).
 - [7] B. T. OCallahan, A. C. Jones, J. H. Park, D. H. Cobden, J. M. Atkin, and M. B. Raschke, Nat. Commun. **6**, art# 6849 (2015).

TABLE I: Constants $\alpha(F)$, β , γ and energy barrier $\Delta G(F)$.

Fluence (mJ/cm ²)	α (J/m ²)	ΔG (J)	ΔG (eV)
0*	100.768136	7.32395E-20	0.457125
0.5*	212.64583	2.77946E-20	0.17348
1*	226.982	2.3089E-20	0.14411
2*	242.33387	1.83834E-20	0.11474
3	251.92034	1.56308E-20	0.09756
4	259.06992	1.36778E-20	0.08537
5	264.85165	1.21637E-20	0.07592
6	269.75703	1.09252E-20	0.06819
7	274.04987	9.87902E-21	0.06166
8	277.89268	8.97219E-21	0.056
9	281.39241	8.1727E-21	0.05101
10	284.61966	7.45813E-21	0.04655
11	287.63047	6.81085E-21	0.04251
12	290.4622	6.21965E-21	0.03882
13	293.14792	5.67651E-21	0.03543
14	295.71281	5.17343E-21	0.03229
15	298.17499	4.70559E-21	0.02937
16	300.55503	4.2666E-21	0.02663
17	302.86532	3.85644E-21	0.02407
18	305.12023	3.46711E-21	0.02164
19	307.33215	3.10021E-21	0.01935
20	309.51173	2.75254E-21	0.01718
21	311.67273	2.42089E-21	0.01511
22	313.82751	2.10526E-21	0.01314
23	315.9896	1.80405E-21	0.01126
24	318.17619	1.51406E-21	0.00945
25	320.40891	1.23848E-21	0.00773
26	322.71763	9.70919E-22	0.00606
27	325.15045	7.14571E-22	0.00446
28	327.79198	4.67836E-22	0.00292
29	330.84847	2.30713E-22	0.00144
30	335.893	0	0

$$\beta = -1.2029353 \times 10^{24} \text{ J/m}^4$$

$$\gamma = 1.077019710 \times 10^{45} \text{ J/m}^6$$

*the constant α and ΔG at $F < 3 \text{ mJ/cm}^2$ are obtained by extrapolation of the experimental data.